Draft version June 23, 2026
Typeset using LaTeX twocolumn style in AASTeX7.0.1

Little Red Dots as Supermassive Analogs of SS 433

Shuying Zhou [1] Mouyuan Sun [1] Xihan Ji [2,3] Ya-Ping Li [4] Luis C. Ho [5,6] Roberto Maiolino [2,3,7] Zhen-Yi Cai [8,9] Hai-Cheng Feng [10,11,12,13] Manqi Fu [1] Wei-Min Gu [1] Tong Liu [1] Junfeng Wang [1] Jianfeng Wu [1] and Yongquan Xue [8,9]

[1] Department of Astronomy, Xiamen University, Xiamen, Fujian 361005, People's Republic of China; msun88@xmu.edu.cn
[2] Kavli Institute for Cosmology, University of Cambridge, Madingley Road, Cambridge CB3 0HA, UK
[3] Cavendish Laboratory, University of Cambridge, 19 JJ Thomson Avenue, Cambridge CB3 0HE, UK
[4] Shanghai Astronomical Observatory, Chinese Academy of Sciences, 80 Nandan Road, Shanghai 200030, People's Republic of China
[5] Kavli Institute for Astronomy and Astrophysics, Peking University, Beijing 100871, People's Republic of China
[6] Department of Astronomy, School of Physics, Peking University, Beijing 100871, People's Republic of China
[7] Department of Physics and Astronomy, University College London, Gower Street, London WC1E 6BT, UK
[8] Department of Astronomy, University of Science and Technology of China, Hefei, Anhui 230026, People's Republic of China
[9] School of Astronomy and Space Science, University of Science and Technology of China, Hefei, Anhui 230026, People's Republic of China
[10] Yunnan Observatories, Chinese Academy of Sciences, Kunming 650216, Yunnan, People's Republic of China
[11] Key Laboratory for the Structure and Evolution of Celestial Objects, Chinese Academy of Sciences, Kunming 650216, Yunnan, People's Republic of China
[12] Center for Astronomical Mega-Science, Chinese Academy of Sciences, 20A Datun Road, Chaoyang District, Beijing 100012, People's Republic of China
[13] Key Laboratory of Radio Astronomy and Technology, Chinese Academy of Sciences, 20A Datun Road, Chaoyang District, Beijing 100101, People's Republic of China

ABSTRACT

High-redshift little red dots (LRDs) are compact sources characterized by V-shaped spectral energy distributions (SEDs), broad emission lines, and often prominent Balmer breaks. Their high number density and apparently large black hole masses suggest that they are essential to the early evolution of galaxies and supermassive black holes (SMBHs); however, the nature of their central engines remains uncertain. Here, we propose that LRDs are the supermassive, high-redshift analogs of the hyper-Eddington accreting Galactic microquasar SS 433, viewed at high inclinations. By scaling the hyper-Eddington accretion physics from stellar-mass black holes to supermassive scales, we show that the observed LRD features, including X-ray weakness, soft optical SEDs, apparent sub-Eddington accretion ratio, and Balmer breaks, emerge naturally from the self-shielding geometry of a puffed-up accretion disk. In this framework, the broad-line regions are ionized by anisotropic radiation escaping from the inner disk, analogous to the unseen UV/X-ray emission revealed by the W50 nebula in SS 433. Their low-inclination or lower-accretion-rate counterparts would appear as little blue dots (LBDs) or normal active galactic nuclei. Our model predicts that the Balmer break strength positively correlates with the broad-line width, that the emission lines are more variable than the optical continuum, that LRDs are intrinsically more luminous than observed, and that LBDs are more variable than LRDs. This unified-scale model redefines LRDs as the essential laboratories for observing the rapid accretion-driven growth that shaped the early assembly of galaxies and their central SMBHs.

Keywords: Accretion (14) — High-redshift galaxies (734) — Quasars (1319) — Supermassive black holes (1663)

1. INTRODUCTION

The James Webb Space Telescope (JWST) has revealed numerous high-redshift galaxies, revising our view of galaxy formation and supermassive black hole

Email: msun88@xmu.edu.cn

(SMBH) evolution. Among them, mysterious little red dots (LRDs) are compact sources with red optical continua, V-shaped spectral energy distributions (SEDs), broad emission lines (BELs), and weak X-ray emission (e.g., Y. Harikane et al. 2023; D. D. Kocevski et al. 2023; M. Perna et al. 2023; J. E. Greene et al. 2024; A. de Graaff et al. 2025a; R. P. Naidu et al. 2025; X. Ji et al. 2025; M.-Y. Zhuang et al. 2026). Some of them exhibit an extremely strong Balmer break that cannot be explained by typical stellar populations (e.g., A. de Graaff et al. 2025b; X. Ji et al. 2025; R. P. Naidu et al. 2025; L. R. Ivey et al. 2026). Several local LRD analogs have also been identified (e.g., X. Ji et al. 2026a; X. Lin et al. 2026a,b). Given their apparently large single-epoch black hole masses ($M_{\rm BH}$) and high number density, LRDs may provide important clues to early SMBH seeding and growth, and their coevolution with host galaxies (e.g., Y. Harikane et al. 2023; Á. Bogdán et al. 2024; R. Maiolino et al. 2024; H. B. Akins et al. 2025; J. Li et al. 2025).

LRDs have attracted extensive theoretical attention, and most models invoke SMBH accretion (see Table 1). Mildly super-Eddington accretion may explain the X-ray weakness (e.g., F. Pacucci & R. Narayan 2024; P. Madau & F. Haardt 2024). The initial explanation for the red optical continuum is the heavy dust extinction; moreover, the lack of submillimetre detection (H. B. Akins et al. 2025; K. Chen et al. 2025) indicates that the dust is compact, possibly circumnuclear (e.g., P. Madau & R. Maiolino 2026; F. Pacucci et al. 2026). Alongside dust reddening, the red optical continuum can also be attributed to either photospheric emission from spherical inflow (e.g., M. C. Begelman et al. 2008; H. Liu et al. 2025; M. C. Begelman & J. Dexter 2026), dense broad-line region (BLR) gas (e.g., X. Ji et al. 2025; P. Madau & R. Maiolino 2026), or stellar processes in self-gravity-dominated disk regions (e.g., C. Zhang et al. 2026; J.-M. Wang et al. 2025a; Y.-X. Chen et al. 2026). Furthermore, the origin of the UV emission remains unclear, with potential contributors from the accretion disk itself (e.g., I. Labbe et al. 2024; C. Zhang et al. 2026; J.-M. Wang et al. 2025a; M. Ando et al. 2026; X. Ji et al. 2026b), scattered disk light, the host galaxy (e.g., J. E. Greene et al. 2024; B. Wang et al. 2024; R. P. Naidu et al. 2025), and the nebula emission (e.g., C.-H. Chen et al. 2025). The prominent Balmer break has been attributed to dense gas in the form of a spherical envelope (M. C. Begelman et al. 2008; D. Kido et al. 2025; H. Liu et al. 2025; M. C. Begelman & J. Dexter 2026) or BLR clouds along the line of sight (e.g., K. Inayoshi & R. Maiolino 2025; X. Ji et al. 2025; R. Maiolino et al. 2025). While the super-Eddington accretion is often favored, the physical nature of LRDs remains unsettled.

SS 433 is probably the only known persistent super-Eddington accretor (e.g., S. N. Fabrika et al. 2007). According to recent mass determinations, the compact object in SS 433 is a stellar-mass black hole with $M_{\rm BH,433} \simeq$ 5–9 $M_\odot$ (A. M. Cherepashchuk et al. 2019). Its dimensionless accretion rate[14] is $\dot{m} \gtrsim 10^{-4}\ M_\odot\ {\rm yr}^{-1}/(2.2 \times 10^{-8}(M_{\rm BH}/M_\odot)\ M_\odot\ {\rm yr}^{-1}) \simeq 500$, placing SS 433 in the hyper-Eddington regime (e.g., A. M. Cherepashchuk 1981). The inclination angle of SS 433 with respect to the orbital axis is $i \simeq 78^\circ$ (i.e., nearly edge on; see, B. Margon & S. F. Anderson 1989; S. S. Eikenberry et al. 2001). Interestingly, the disk UV/optical emission (3000 Å–7000 Å) of SS 433 can be well modeled by a blackbody function with the effective temperature of 5×10^4–7×10^4 K (J. F. Dolan et al. 1997), much softer than the theoretical expectation ($\sim 10^7$ K). In addition, SS 433 is undetectable at UV wavelengths of $\lesssim 2000$ Å (D. R. Gies et al. 2002). The physical mechanism that drives the soft SED in SS 433 may also be responsible for the red optical continuum observed in LRDs.

Previous observational (e.g., E. P. J. van den Heuvel 1981) and theoretical (e.g., A. R. King et al. 2000) studies have suggested that SS 433 launches strong winds with a mass outflow rate comparable to the accretion rate. Such winds can be optically thick, with a large scattering optical depth $\tau_{\rm es} \sim 100$, and thus soften the underlying disk emission throughout the wind (panel b in Figure 1; e.g., M. C. Begelman et al. 2006). The wind photosphere then sets the observed disk SED, which is approximately a blackbody with $T_{\rm eff} \sim 10^5$ K. This SED is much softer than expected from a bare accretion disk. The same picture has also been invoked for ultraluminous X-ray sources (ULXs, seen close to face-on; for a recent review, see, e.g., P. Kaaret et al. 2017; A. King et al. 2023) and their supersoft counterparts at high inclinations, i.e., ultraluminous supersoft sources (ULSs; e.g., A. R. King & K. A. Pounds 2003; R.-F. Shen et al. 2015; R. Soria & A. Kong 2016).

The accretion rate of a black hole can far exceed the Eddington accretion limit $\dot{M}_{\rm Edd}$, and advection due to "photon trapping" (M. C. Begelman 1978) is important (see, e.g., M. A. Abramowicz et al. 1988; L. Zhang et al. 2025). The flow should therefore consist of an outer standard thin disk (SSD; N. I. Shakura & R. A. Sunyaev 1973) and a geometrically thick inner disk (hereafter the SLIM disk) inside a truncation radius $R_{\rm tr}$. This radius, which increases with $\dot{m}$ (M. A. Abramowicz et al. 1988),

[14] We define $\dot{m} \equiv \dot{M}/\dot{M}_{\rm Edd}$, with $\dot{M}_{\rm Edd} = 10 L_{\rm Edd}/c^2$.

is often close to the "spherization" radius defined by N. I. Shakura & R. A. Sunyaev (1973), where strong winds are launched. For self-consistency, the thermalization radius in the wind scenario must exceed $R_{\rm tr}$, implying an outflow rate of $\dot{m} \gtrsim 500$ (e.g., R. Soria & A. Kong 2016). If $\dot{m} \ll 500$, the winds should be too optically thin to thermalize the high-energy disk emission. Even then, self-shielding by the puffed-up thick disk can block the hard photons, so a ULX may still appear as a ULS at $i \gtrsim 45°$ (panel a in Figure 1; W.-M. Gu et al. 2016). SS 433 also fits into this picture because of its high inclination and hyper-Eddington accretion rate.

Observations of SS 433 and its surrounding W50 nebula provide convincing evidence that its hyper-Eddington accretion produces highly anisotropic UV and X-ray emission. First, optical spectra of gas filaments in the W50 nebula exhibit He II, Hβ, and [O III] emission lines, indicating strong unseen ionizing continua of $\sim 10^{40}$ erg s^{-1} from SS 433 (S. N. Fabrika & O. Sholukhova 2008), which is about two orders of magnitude larger than the detected optical emission from the edge-on sightline. Second, broadband X-ray observations reveal the strong unseen X-ray emission from SS 433 (M. J. Middleton et al. 2021). Hence, while an observer at a high inclination only sees the self-shielded soft red continuum, gas in polar regions is fully exposed to high-energy ionizing radiation escaping from the innermost regions. The same anisotropy may also be found in hyper-accretion SMBHs.

Motivated by the softer-than-expected emission and extreme anisotropic radiation in SS 433, we propose a hyper-Eddington accretion structure for SMBHs in LRDs. The soft emission in LRDs manifests as the observed red optical continuum, which can be roughly fitted by a modified blackbody with $T_{\rm eff} \approx 5000$–7000 K (but see e.g., A. de Graaff et al. 2025a, for potential revisions of the blackbody model). Meanwhile, the anisotropic ionizing radiation, analogous to the unseen UV/X-ray emission in SS 433, illuminates the BLR clouds, naturally producing the BELs in LRDs. The radiative transfer of dense but cold gas (e.g., H. Liu et al. 2025) in the disk surface can create the strong Balmer break observed in some LRDs (e.g., X. Ji et al. 2025). We therefore interpret LRDs as hyper-Eddington SMBHs viewed at high inclination angles.

The manuscript is organized as follows: Section 2 describes our hyper-Eddington accretion model, its comparisons with observations, and implications; Section 3 compares our model with others and explores its broader physical implications. The main conclusions are summarized in Section 4. We adopt the flat ΛCDM cosmology with $H_0 = 70$ km s^{-1} Mpc^{-1}, $\Omega_{\rm m} = 0.3$, and $\Omega_\Lambda = 0.7$ in the manuscript. We denote $r = R/R_{\rm S}$ as the radial distance from the SMBH in units of the Schwarzschild radius $R_{\rm S} = 2GM_{\rm BH}/c^2$.

2. THE IDEA

2.1. *Hyper-Eddington accretion: from stellar-mass to supermassive black holes*

Following the framework in SS 433, we consider a hyper-Eddington accretion flow consisting of an outer standard SSD and an inner SLIM disk within $R_{\rm tr}$ (panel d in Figure 1). Due to the significant advection cooling and intense radiation pressure at hyper-Eddington accretion rates, the inner SLIM disk is puffed up to be geometrically thick, with a scale height H comparable to the radius $R = rR_{\rm S}$. Analytic work suggests that H can even exceed R (e.g., W.-M. Gu et al. 2009; W.-M. Gu 2012). We define $R_{\rm tr}$ as the photon-trapping radius, which is determined by the condition that the vertical diffusion timescale, $t_{\rm diff} = 3H\tau_{\rm mid}/c$, is equal to the accretion timescale, $t_{\rm acc} = R/V_R$, where $\tau_{\rm mid}$, V_R and c denote the midplane optical depth, the radial velocity and speed of light, respectively. In the electron scattering dominated regime ($\kappa_{\rm tot} \simeq \kappa_{\rm es}$), the transition radius scales as $R_{\rm tr} = 15\dot{m}(H/R)R_{\rm S} \simeq 15\dot{m}R_{\rm S}$ (J.-M. Wang & Y.-Y. Zhou 1999; S. Kato et al. 2008). For the outer SSD region, the effective temperature profile is given by

$$T_{\rm eff,out} = \left(\frac{3GM_{\rm BH}\dot{M}f}{8\pi\sigma_{\rm SB}R^3}\right)^{1/4}, \tag{1}$$

we set the factor $f = 1 - \sqrt{R_{\rm ISCO}/R} \simeq 1$ in the following analysis because $R \gg R_{\rm ISCO}$ (with $R_{\rm ISCO} = 3R_{\rm S}$ for a Schwarzschild black hole). At the truncation radius $R = R_{\rm tr}$, the effective temperature is

$$T_{\rm eff,tr} = 8000\ [{\rm K}] \times (M_{\rm BH}/[10^6 M_\odot])^{-0.25}(\dot{m}/1000)^{-0.5}. \tag{2}$$

If mass loss is negligible, the effective temperature profile of the inner SLIM disk is flatter than that of the SSD because a significant fraction of the viscous heat is advected into the black hole rather than being radiated. The effective temperature of the inner SLIM disk can be expressed as (e.g., S. Kato et al. 2008)

$$T_{\rm eff,in} = T_{\rm eff,tr}\left(\frac{R}{R_{\rm tr}}\right)^{-0.5} = 10^6\ [{\rm K}]\, r^{-0.5}\left(\frac{M_{\rm BH}}{10^6 M_\odot}\right)^{-0.25}. \tag{3}$$

Note that the accretion rate of the SLIM disk is assumed to be constant. In reality, the inner SLIM disk can drive powerful jets, and a considerable fraction of the accretion power may be released as the mechanical energy of the jets. Consequently, the effective temperature should be lower than that given by Eq. 3. Hence,

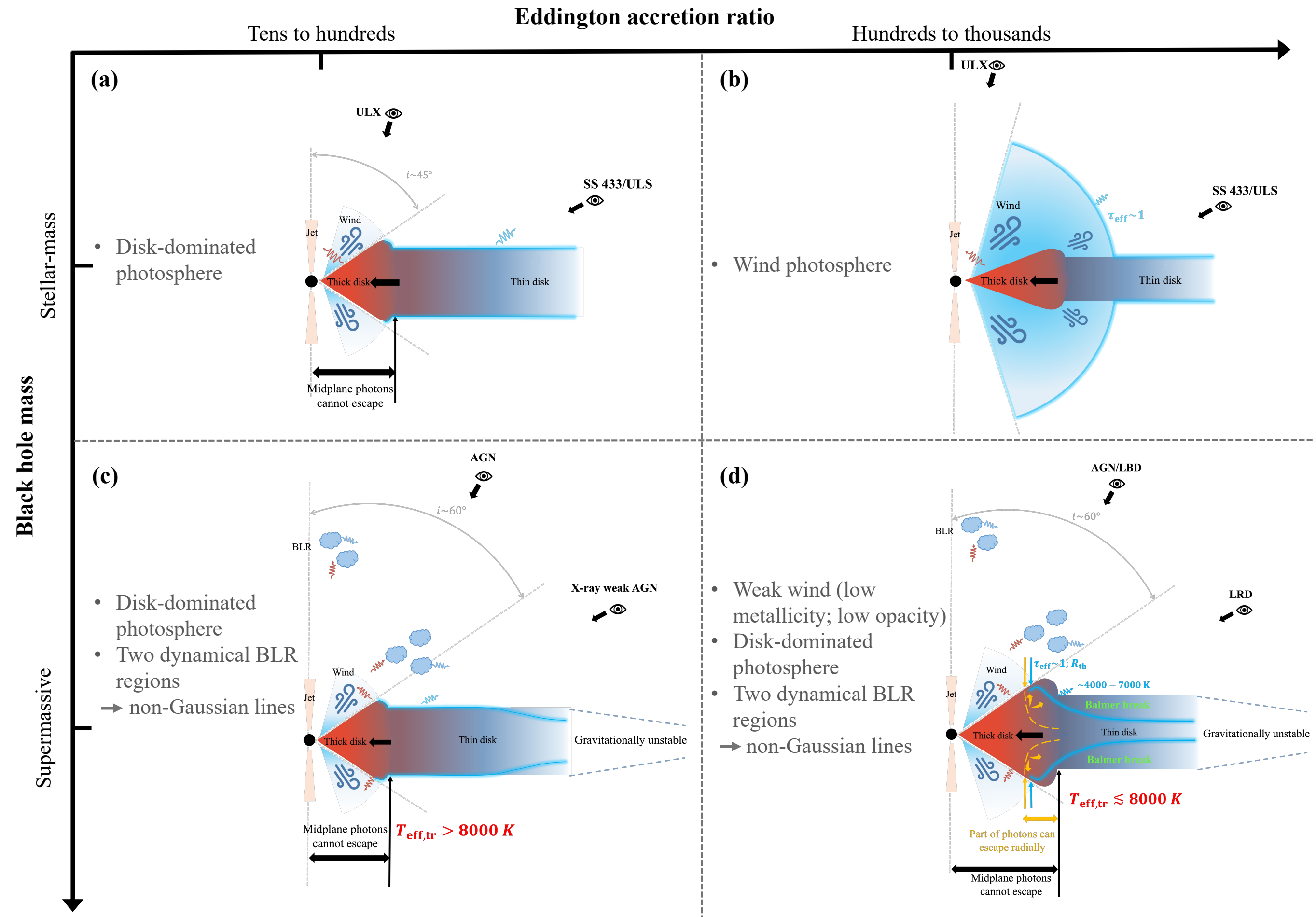

Figure 1. Schematic view of the central-engine models for LRDs, SS 433, and ULSs across different black hole masses and Eddington accretion ratios. For stellar-mass black holes, a hyper-Eddington accretion disk with $T_{\rm eff} \gg 10^4$ K and opacity ~ 0.34 cm^2 g^{-1} can launch strong radiation-driven winds. At $\dot{m} \gtrsim 500$ (panel b), the wind is optically thick and yields a soft SED, as in SS 433 and some ULSs; at $\dot{m} \simeq 10$ (panel a), the wind is optically thin, but self-shielding still allows either hard or soft SEDs depending on inclination. Similar behavior is expected for SMBHs with $M_{\rm BH} = 10^6$–10^8 $M_\odot$ at $\dot{m} \simeq 10$ (panel c). At $\dot{m} \gtrsim 500$ (panel d), however, the thick-disk surface temperature drops below ~ 8000 K, triggering hydrogen recombination, sharply reducing the opacity, and suppressing strong radiation pressure-driven winds. Part of the thick disk then becomes transparent, and emission from the outer regions produces the optical continuum and Balmer break in LRDs. At low inclination, the full thick-disk emission is visible, yielding an LBD-like SED. The BLR clouds are ionized by the highly anisotropic ionization field.

comparing with a hyper-accretion stellar black hole with $M_{\rm BH} \sim 10 M_\odot$, the same disk with $M_{\rm BH} \gtrsim 10^6 M_\odot$ has a much lower temperature and can barely produce sufficient hard ionizing photons ($\gtrsim 50$ eV) to excite strong high-ionization lines such as He II (e.g., M. Tang et al. 2025; M. Brazzini et al. 2026), albeit it can generate ~ 10 eV to ionized hydrogen. Meanwhile, the self-shielding structure effectively reduces the ionizing continuum that illuminates the high-inclination BLR clouds, further eliminating the high-ionization BELs.

Previous studies suggest that SMBH accretion at $\dot{m} \sim 500$ can overcome radiative feedback (e.g., K. Inayoshi et al. 2016) and may not drive winds if the infalling gas has a sufficiently low specific angular momentum (M. C. Begelman & M. Volonteri 2017). Then, the disk remains geometrically thick out to thousands of $R_{\rm S}$, where the surface temperature at truncation radius $R_{\rm tr}$ drops to $T_{\rm eff,tr} = 8000$ [K] (Eq. 2). At this temperature, both electron-scattering and true-absorption opacities drop sharply because of hydrogen recombination. The reduced opacity makes the radiation pressure too weak to launch powerful radiation-pressure-driven winds near $R_{\rm tr}$. While line-driven winds could potentially exist, their strength depends critically upon the gas metallicity (K. G. Gayley 1995). Thus, in low-metallicity environments, which are potentially associated with high-redshift LRDs (e.g., B. Trefoloni et al. 2025; L. R. Ivey et al. 2026; R. Maiolino et al. 2026), the line force multiplier may be significantly reduced, resulting in a much lower mass-loss rate than in high-metallicity environments (J. I. Castor et al. 1975; D. Proga 1999). This expectation is consistent with the lack of significant, large-scale outflows observed in high-redshift AGNs (R. Maiolino et al. 2025). In addition, the BLR reverberation mapping of super-Eddington-accreting black holes in the local universe reveals a lack of universal blueshifted outflow signatures, with some instead exhibiting evidence of infalling gas in the BLR (e.g., P. Du et al. 2016), which also supports the idea that winds are not universally produced in SMBH super-Eddington systems. Therefore, the wind-dominated scenario of SS 433/ULSs[15] may not be directly applicable to LRDs; nevertheless, SS 433 and LRDs can be unified within a hyper-Eddington framework. In our LRD model, the UV/optical continuum is shaped by geometric self-shielding from the inflated SLIM disk itself, as evidenced by low-velocity redshifted/blueshifted absorption in the Balmer lines (e.g., J. Matthee et al. 2026; A. Torralba et al. 2026).

At high inclination angles, the puffed-up geometry of the inner SLIM disk self-shields the innermost accretion flow significantly (panel d of Figure 1). This leads to highly anisotropic and inclination-dependent SEDs, as discussed for BHXRBs (K.-Y. Watarai et al. 2005) and AGNs (J.-M. Wang et al. 2014). The same effect has also been proposed to explain the observed X-ray weakness of LRDs (e.g., P. Madau & F. Haardt 2024), although those models are based on the "Polish doughnut" (e.g., B. Paczyńsky & P. J. Wiita 1980) rather than the SLIM disk. In such models, the innermost X-ray and extreme-ultraviolet emission are obscured unless the line of sight is nearly face-on. Furthermore, the intrinsic X-ray emission is expected to be suppressed at high accretion rates due to enhanced Compton cooling (e.g., C. Done et al. 2007; P. Madau & F. Haardt 2024).

According to Eq. 2, we expect a typical LRD temperature of $5 \times 10^4 \ (M_{\rm BH,LRD}/M_{\rm BH,433})^{-0.25} C$ [K] $\simeq 3000\,(M_{\rm BH,LRD}/[10^6 M_\odot])^{-0.25} C$ [K], where $C = (r_{\rm tr,LRD}/r_{\rm tr,433})^{-0.5}$. For LRDs hosting SMBHs with $M_{\rm BH} \approx O(10^6) M_\odot$ (e.g., J.-M. Wang et al. 2025a), our disk model naturally accounts for the ~ 5000 K optical continua (for details, see Section 2.2). With such a cold temperature, the dense gaseous disk is responsible for the Balmer break (for details, see Section 2.3).

[15] The self-shield disk may also contribute to the observed soft spectrum.

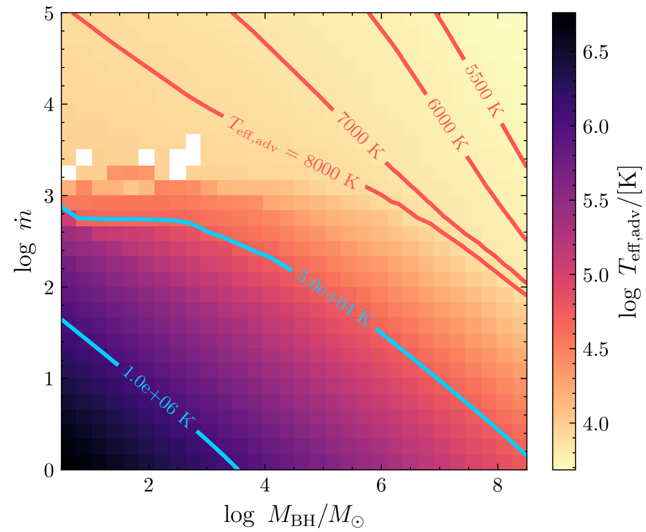

Figure 2. Disk surface temperature at the innermost radius ($R_{\rm adv}$) visible along a high-inclination sightline (i.e., $\sim 90°$). At this radius, the advection timescale equals the radial photon diffusion timescale. Note that the solutions in the white pixels are numerically unstable. The two cyan curves correspond to the observed effective temperatures of SS 433 (S. N. Fabrika et al. 2007) and ULSs. The four red curves show typical effective temperatures for LRDs. For SMBHs with $\dot{m} \gtrsim 500$, the maximum visible inner-disk temperature is 5000–8000 K, similar to that inferred for LRDs.

2.2. *The red optical continuum*

To evaluate the maximum observable temperature of the disk, we use a 1D toy model focusing on the advective photon trapping radius ($R_{\rm adv}$), where the radial photon diffusion timescale is equal to the accretion timescale ($t_{\rm diff,radial} \simeq t_{\rm acc}$). For an extremely large inclination angle (i.e., $\sim 90°$), the surface emission from inner regions is advected to the central SMBH, resulting in $R_{\rm adv}$ being the innermost visible radius. At that radius, the corresponding surface temperature is the maximum observable temperature. The radial diffusion timescale is expressed as $t_{\rm diff,radial} \simeq 3R(\kappa_{\rm R}\rho R)/c$ (S. Kato et al. 2008), where $\kappa_{\rm R}$ and $\rho = \dot{M}/(4\pi R H |V_{\rm R}|)$ denote the total Rosseland-mean opacity (i.e., the gray approximation) of the SLIM disk and the gas density at radius R, respectively. We use the `NuPac` code (J. Morag 2025a,b) to generate high-frequency-resolution and Rosseland-mean opacity tables with a low metallicity of $Z = 0.005 Z_\odot$ (B. Trefoloni et al. 2025; L. R. Ivey et al. 2026; X. Lin et al. 2026a; R. Maiolino et al. 2026). The accretion timescale is estimated by $t_{\rm acc} \simeq R/|V_{\rm R}|$, where $|V_{\rm R}| \simeq \beta\sqrt{GM_{\rm BH}/R}$ is the radial inflow velocity. The value of β is uncertain and depends on the viscous transport efficiency within the accretion disk; here, we adopt $\beta = 0.044$ (J.-M. Wang & Y.-Y. Zhou 1999). Hence, $\kappa_{\rm R} = (c/(3\beta\sqrt{GM_{\rm BH}/R}))(1/(\rho R))$.

For a given $M_{\rm BH}$ and $\dot{m}$, we obtain the characteristic temperature by solving $t_{\rm diff,radial} = t_{\rm acc}$ (Figure 2). In the stellar-mass black hole regime, we obtain 10^4 (10^6) K for $\dot{m} \sim 500$ ($\dot{m} \sim 30$), in agreement with SS 433 and ULSs, respectively. We note that for stellar-mass black holes, the dramatic change of opacity due to the partially ionized hydrogen may potentially cause the solution to be unstable for $\dot{m} \sim 1500$–4000. In the SMBH regime, the opacity $\kappa_{\rm R}$ becomes extremely sensitive to the gas temperature (with $\kappa \sim T^{\sim 13}$; see, e.g., H. Liu et al. 2025). Consequently, the maximum observable effective temperature at high inclination depends only weakly on ρ (and thus on $\dot{m}$) or $M_{\rm BH}$. For SMBHs with $\dot{m} \gtrsim 500$, this temperature is constrained to 5000–8000 K, consistent with LRD observations (see, e.g., figure 3 in A. de Graaff et al. 2025a). The geometric self-shielding effectively obscures the UV emission from the inner disk with $T > 8000$ K, and the sharp drop in opacity restricts the maximum observable temperature for SMBHs to 5000–8000 K, thereby naturally producing the red optical continuum in LRDs.

If the inclination angle is low and/or $\dot{m} \ll 100$ for SMBHs, one can directly detect emission from inner regions. Then, the system appears as little blue dots (LBDs; M. Brazzini et al. 2026), which have a blue SED, high-ionization BELs, and lack the Balmer break (see Section 2.3). LBDs should be X-ray weak due to high Eddington accretion ratios.

2.3. *Emergent SED and the Balmer break*

As pointed out by a number of previous works (e.g., K. Inayoshi & R. Maiolino 2025; X. Ji et al. 2025; H. Liu et al. 2025; M. C. Begelman & J. Dexter 2026), the Balmer break observed in some LRDs can be naturally attributed to the rapid decline in opacity between the rest-frame wavelengths of 3600 Å and 4000 Å for a temperature of $\lesssim 10^4$ K. This is because hydrogen atoms with a principal quantum number of $n = 2$ efficiently absorb photons with rest-frame wavelengths shorter than the Balmer limit of $\lambda \approx 3646$ Å. Quantifying this effect requires solving the radiative transfer equations within the hyper-Eddington accretion disk.

As a first step, we obtain the vertical structure of the accretion disk by solving the hydrostatic equilibrium, energy balance, and radiative transfer equations (see Appendix A). In our calculations, we adopt a fiducial value of the dimensionless viscosity $\alpha = 0.1$ unless otherwise specified. An example of the resulting vertical structure is shown in Figure 3. Here, the total and effective optical depths are defined as $\tau_{\rm tot} = \int_z^H \kappa_{\rm R}\rho dz$ and $\tau_{\rm eff} = \int_z^H \sqrt{\kappa_{\rm R}\kappa_{\rm abs}}\rho dz$ with $\kappa_{\rm abs}$ is the true absorption opacity, respectively. A substantial fraction of the outer disk is optically thin, with $\tau_{\rm tot} < 1$ or $\tau_{\rm eff} < 1$, and is therefore also transparent to emission from adjacent inner regions. The thermalization surface ($\tau_{\rm eff} = 1$) is located in a regime with gas densities of $\sim 10^{-12}$–10^{-11} g cm^{-3} and temperatures of ~ 7000 K. As shown in the final panel of Figure 3, this thermalization surface closely aligns with the region where the opacity ratio $\kappa_{\rm eff,4000Å}/\kappa_{\rm eff,3600Å}$ reaches its minimum. As this ratio serves as a proxy for Balmer break production, its alignment with the thermalization surface ensures that the emergent SED is shaped by the sharp opacity discontinuity at the Balmer limit, providing a robust mechanism for producing prominent Balmer breaks.

Building upon the derived disk vertical structures, we compute the emergent SED by solving the frequency-dependent radiative transfer equation in a two-dimensional (r, z) configuration. We assume local thermodynamic equilibrium (LTE) and consider true absorption and isotropic electron scattering. The radiative transfer equation is given by

$$\frac{dI_\nu}{ds} = \chi_\nu(S_\nu - I_\nu), \tag{4}$$

where I_ν is the specific intensity, S_ν is the source function, ds is the path length along a ray, and $\chi_\nu = \rho(\kappa_{{\rm abs},\nu} + \kappa_{\rm es})$ is the total extinction coefficient. Under LTE and in the presence of scattering, the source function is coupled to the mean intensity J_ν via $S_\nu = (1-\epsilon_\nu)J_\nu + \epsilon_\nu B_\nu$, where $\epsilon_\nu = \kappa_{{\rm abs},\nu}/(\kappa_{{\rm abs},\nu} + \kappa_{\rm es})$ and B_ν is the Planck function. Detailed descriptions are provided in Appendix B.

The observed monochromatic luminosity for a given inclination i is obtained by integrating the emergent intensity over the visible surfaces of the near and far (relative to the observer) sides of the disk (see Appendix B). The resulting SED for an SMBH with $M_{\rm BH} = 10^7 M_\odot$ and $\dot{m} = 1000$ is shown in Figure 4. The spectrum is well-approximated by a blackbody with $T_{\rm eff} = 6000$ K, and the Balmer break is clearly visible in high-inclination cases with $i \gtrsim 60°$. This is due to severe geometric obscuration of the inner disk at large angles. The high-temperature UV emission is blocked by the "puffed-up" disk, making the Balmer break from the cooler outer radii more visible.

Our radiative transfer models also produce emission lines (e.g., SED with an inclination angle of 80° in Figure 4). Within the scattering-dominated layers, the underlying continuum radiation is significantly diluted; however, the emission lines remain optically thick and effectively thermalize with the local gas. Consequently, the emission lines stand out against the diluted local

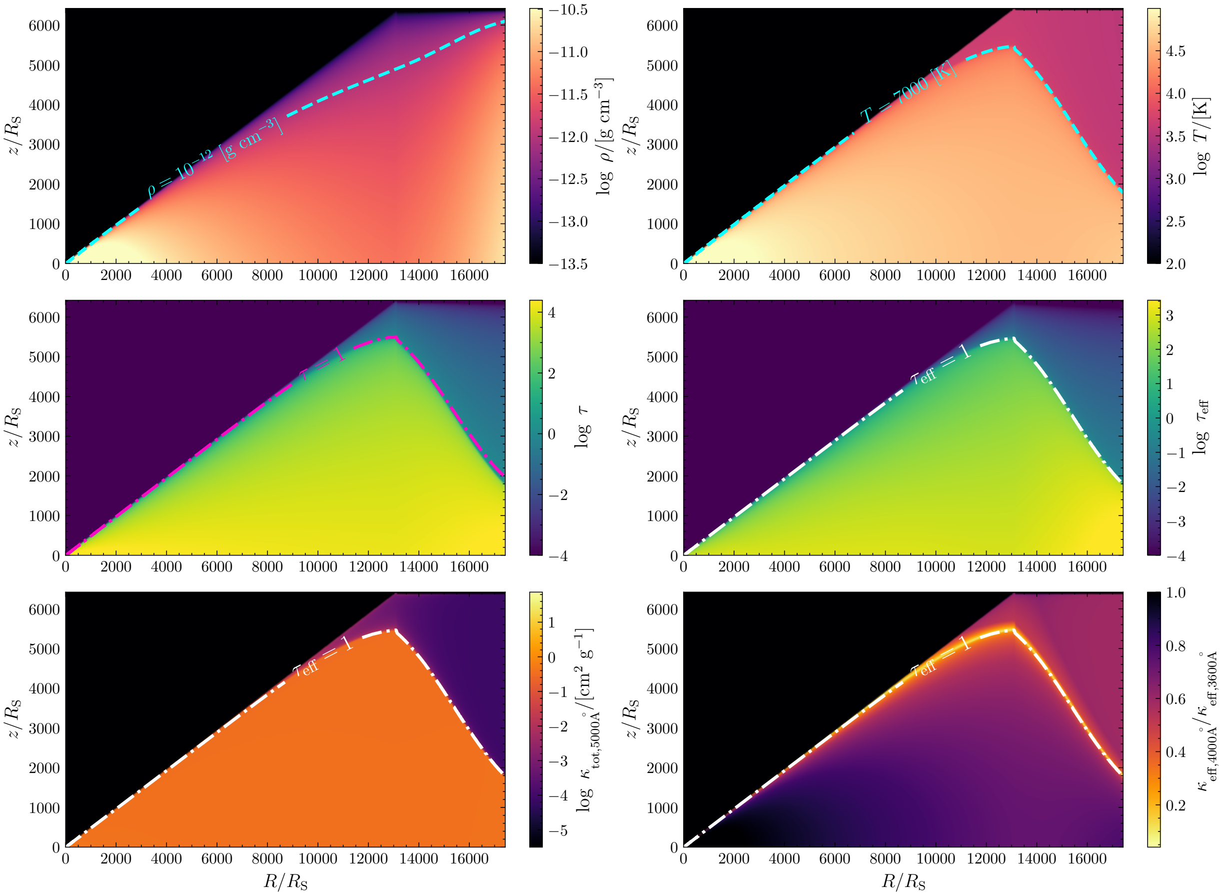

Figure 3. Vertical structure of a hyper-Eddington accretion disk around an SMBH with $M_{\rm BH} = 10^7 M_\odot$ and $\dot{m} = 1000$. The six panels show the gas density (ρ), temperature (T), face-on total optical depth (τ), face-on effective optical depth ($\tau_{\rm eff}$), total opacity at 5000 Å ($\kappa_{\rm tot,5000Å}$), and the effective opacity ratio between 4000 Å and 3600 Å ($\kappa_{\rm eff,4000Å}/\kappa_{\rm eff,3600Å}$), respectively. The ratio $\kappa_{\rm eff,4000Å}/\kappa_{\rm eff,3600Å}$ serves as a proxy for the production of Balmer breaks; the region of maximum Balmer break production (indicated by the yellow color in the final panel) aligns closely with the thermalization surface ($\tau_{\rm eff} = 1$).

continuum. A similar process was also proposed for cataclysmic variables (e.g., R. E. Williams 1980). We expect the emission lines originating from the accretion disk to have broad profiles, with velocity widths of several thousand kilometers per second caused by Keplerian rotation, and slight shifts induced by gas inflow from near (redshifted) and far (blueshifted) sides (see Appendix B). However, we note that the exact line fluxes and profiles of these lines depend upon non-LTE effects, which are beyond the scope of this work. We expect that these lines are weaker than BELs from BLRs and are undetectable.

While our static radiative transfer calculations yield relatively sharp spectral features at the Balmer limit, kinematic broadening from gas turbulence in the accretion disk can smooth these edges. Accurately reproducing the intricate features of observed spectra requires the incorporation of kinematic information into radiative transfer frameworks, which is beyond the scope of this work.

We present a qualitative comparison between simulated emergent SEDs and observations in Figure 5. Based on the LRD-to-total flux fraction estimations in W. Q. Sun et al. (2026), we randomly select four sources with the LRD flux fraction at 5500 Å larger than 80%. CAPERS 11585 and 19799 were observed as part of the CAPERS survey (GO-6368; PI: M. Dickinson). JADES-GND-28074, one of the most well-characterized nearby LRDs at $z = 2.26$ (I. Juodžbalis et al. 2024), was observed by the JADES program (GO-1811; M. J. Rieke et al. 2023; A. J. Bunker et al. 2024; F. D'Eugenio et al. 2025; D. J. Eisenstein et al. 2026). The NIRSpec/PRISM spectroscopic data for these three sources are retrieved from the DAWN JWST Archive (version 4.4[16]; G. Brammer & F. Valentino 2025), with data processing described in A. de Graaff et al. (2025c) and K. E. Heintz et al. (2025), and incorporating the v4 improve-

[16] https://dawn-cph.github.io/dja/spectroscopy/nirspec/

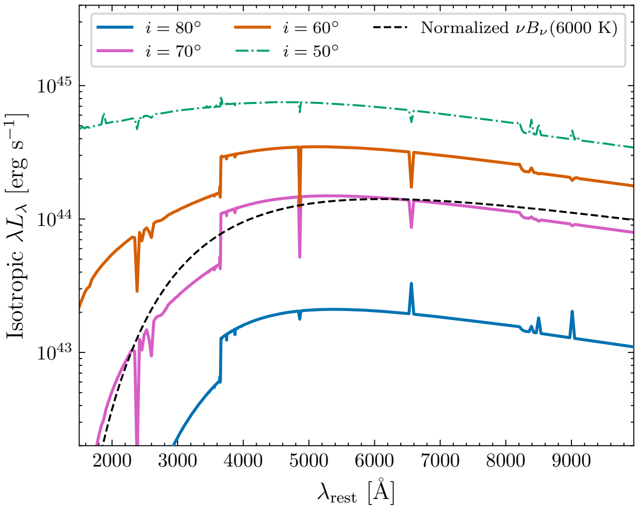

Figure 4. Emergent SED for an SMBH with $M_{\rm BH} = 10^7 M_\odot$ and $\dot{m} = 1000$ at different inclinations, obtained through radiative transfer simulations with the disk vertical structure in Figure 3. While the spectra are well-approximated by a normalized 6000 K blackbody (black dashed curve), a distinct Balmer break emerges at high inclinations ($\gtrsim 60°$).

ments detailed by F. Valentino et al. (2025) and C. L. Pollock et al. (2026). Additionally, we include Abell-2744-QSO1, a strongly lensed LRD at $z = 7.04$ (e.g., L. J. Furtak et al. 2024; X. Ji et al. 2025). The spectrum presented here is derived from image A (X. Ji et al. 2025), which is reduced using NIRSpec/PRISM Micro-Shutter Assembly data and the GTO pipeline reduction method described in J. Scholtz et al. (2025). To account for the gravitational lensing effect of this source, we apply a magnification correction factor of $\mu = 6$ (X. Ji et al. 2025). The model-to-data comparison presented here should be regarded as a demonstration rather than a rigorous SED fit (i.e., without fine-tuning). As shown in the left panel of Figure 5, the emergent SEDs of an SMBH with $M_{\rm BH} = 10^7 M_\odot$ and $\dot{m} = 1000$ at high inclinations are broadly consistent with observed red continua and Balmer breaks. To further improve the agreement between the model and the observed data, we incorporate the D. Calzetti et al. (2000) attenuation law (right panel of Figure 5) with a modest amount of dust extinction of $A_V \lesssim 1.5$ mag.

Prominent Balmer breaks that cannot be explained by the typical stellar population have been detected in some LRDs (e.g., X. Ji et al. 2025; A. de Graaff et al. 2025a; R. P. Naidu et al. 2025), providing important clues about the physical conditions in emission regions. We quantify the Balmer break strengths of simulated emergent SEDs with different black hole masses and Eddington accretion ratios and compare them with observations in Figure 6. While A. de Graaff et al. (2025a) define the Balmer break strength using the flux ratio between two rest-frame wavelength windows ([3620, 3720] Å and [4000, 4100] Å), we adopt a monochromatic flux ratio $f_{4000\rm Å}/f_{3600\rm Å}$ between the line-free wavelength 4000 Å and 3600 Å to characterize the Balmer break strength of simulated SEDs. As shown in the left panel of Figure 6, the Balmer break strength generally increases with inclination angles. This trend is caused by the fact that higher inclinations provide a more obscured view of the hot inner disk, allowing the cool ($T \lesssim 10^4$ K), dense outer regions to dominate the emergent spectrum. The right panel of Figure 6 shows the break strength as a function of the monochromatic luminosity at 5100 Å. Observations from A. de Graaff et al. (2025a) are broadly consistent with our hyper-Eddington accretion model predictions. In addition, we test the impact of the viscosity parameter α on the Balmer break strength. We find that adopting a smaller viscosity parameter ($\alpha = 0.01$) modifies the vertical structure of the disk, resulting in a more pronounced Balmer break strength than with $\alpha = 0.1$ (see Appendix C).

2.4. *The broad emission lines*

In our hyper-Eddington accretion model, BLR clouds in the polar regions are photoionized by UV photons from the inner SLIM disk, producing the observed BELs (panel d in Figure 1). This geometry naturally produces broad Lyα through ionization photons in polar directions (e.g., X. Ji et al. 2026b). A large number of BLR clouds can form near the equatorial direction. Because of significant self-shielding in the puffed-up SLIM disk, the ionizing radiation field is highly anisotropic: polar clouds receive substantially more UV photons than equatorial clouds. Hence, the polar clouds that are most efficient at producing BELs should also be located further away than equatorial clouds, which is consistent with BLR stratification. In the simplest case, the BEL profile can be described as the superposition of high- and low-velocity Gaussian components, which together resemble a Lorentzian profile or an exponential profile (e.g., J.-M. Wang et al. 2014; J. Scholtz et al. 2026; P. Madau et al. 2026). In the local universe, narrow-line Seyfert 1 galaxies, some of which are likely powered by super-Eddington accretion onto relatively small SMBHs, often show Lorentzian BEL profiles (e.g., H. Zhou et al. 2006; M. Berton et al. 2020) and can be understood in the same framework (J.-M. Wang et al. 2014). Interestingly, a large fraction of LRDs are well characterized by Lorentzian or two-Gaussian profiles. While such non-Gaussian features have recently been interpreted as signatures of electron scattering in dense gas (e.g., S.-J. Chang et al. 2026; V. Rusakov et al. 2026), we argue

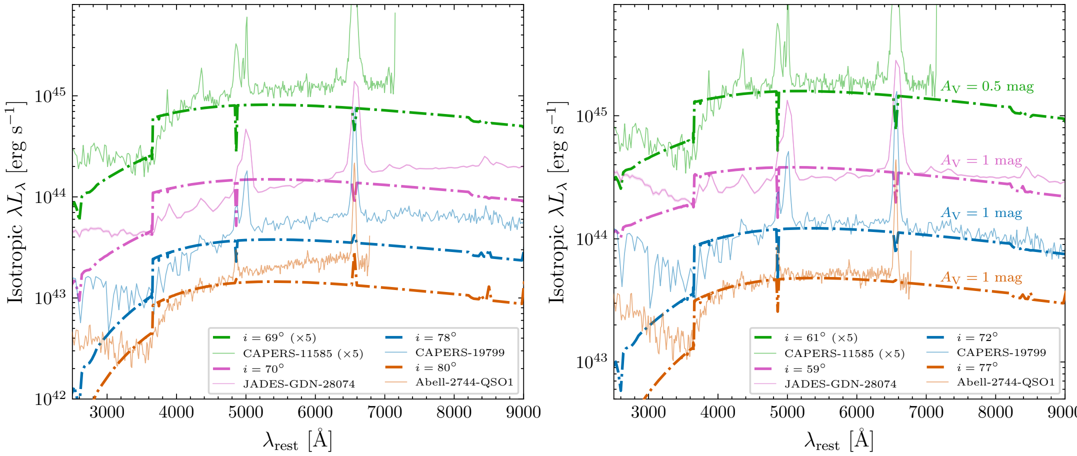

Figure 5. Qualitative comparison of observations and simulations. The dashed curves show model SEDs for an SMBH with $M_{\rm BH} = 10^7 M_\odot$ and $\dot{m} = 1000$ at various inclination angles. The solid curves and shaded regions represent observations with their 1σ uncertainties. In the right panel, we apply the D. Calzetti et al. (2000) dust attenuation law, with varying extinction coefficients, to "deredden" the observations. Observations with low dust extinction roughly match our model predictions.

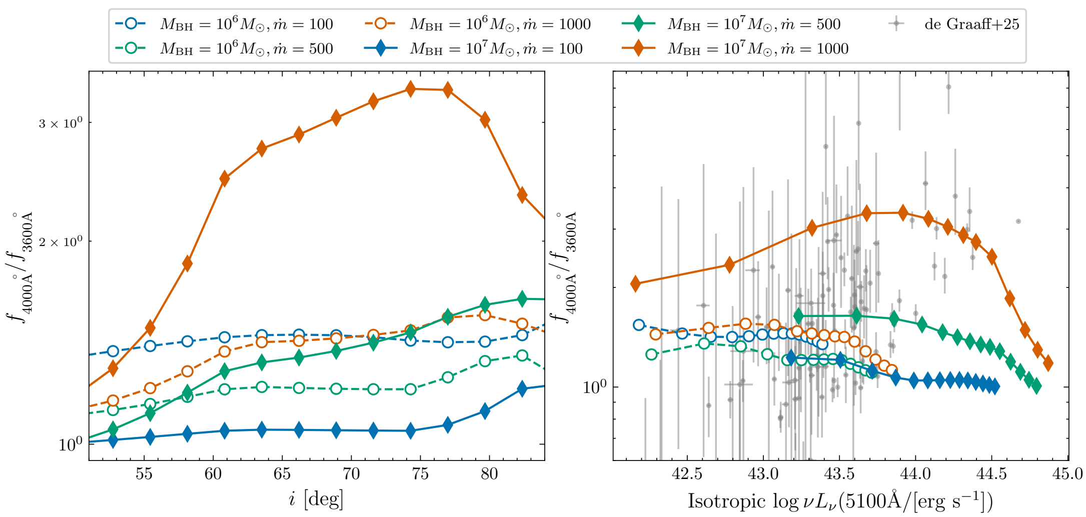

Figure 6. Balmer break strength ($f_{4000\text{Å}}/f_{3600\text{Å}}$) as a function of inclination angle and monochromatic luminosity at 5100 Å. Open circles and filled diamonds represent SMBHs with $M_{\rm BH} = 10^6 M_\odot$ and $10^7 M_\odot$, respectively. Blue, green, and orange markers indicate accretion rates $\dot{m} = 100$, 500, and 1000, respectively. In the right panel, gray dots denote observational data from A. de Graaff et al. (2025a), with error bars representing 1σ uncertainties. The Balmer break strength generally increases with inclination angle, and the observational data are broadly consistent with our simulations.

that these profiles arise naturally from BLRs in super-Eddington systems (see also M. Brazzini et al. 2025, 2026; J. Scholtz et al. 2026; P. Madau et al. 2026).

If the BLR clouds follow a disk-like Keplerian velocity field, a high inclination angle will naturally correspond to a large line-of-sight velocity, resulting in broader lines. Our model therefore predicts a positive correlation between Balmer break strength and the full width at half maximum (FWHM) of the BELs, as tentatively observed by J. Matthee et al. (2026). Consequently, single-epoch black hole mass estimators calibrated on low-inclination type-1 AGNs may introduce an inclination-dependent bias when applied to LRDs. Assuming a mean inclination of 30° for type-1 AGNs and 75° for LRDs, the inclination effect induces an overestimation factor of $(\sin 30°/\sin 75°)^2 \approx 3.7$. For LRDs with Balmer breaks, the rest-frame 5100 Å luminosity may be a useful empirical proxy for black hole mass.

We also briefly discuss the equivalent widths (EWs) of BELs. The observed EW traces the ratio of the line flux to the local continuum flux. The line flux is proportional to the number of ionizing photons intercepted by the BLR clouds, while the observed continuum is highly anisotropic due to the geometric self-shielding of the puffed-up SLIM disk. Consequently, at large inclination angles, the observed optical continuum flux is suppressed, which is consistent with the observed optical luminosity falling below local relation expectations (C.-H. Chen et al. 2026), ultimately resulting in an increased EW of Hα. Due to the anisotropic ionizing structure of BLRs and the intrinsic deficiency of high-energy ionizing photons in hyper-Eddington accretion disks, the broad He II in LRDs and LBDs should be weak or absent. These effects have been well demonstrated by P. Madau & R. Maiolino (2026).

2.5. *The optical variability*

In our hyper-Eddington accretion model, the red optical continuum of LRDs is produced by the self-shielded disk at the typical radius of $10^4\ R_S$. Due to the large accretion rate and radius, the local thermal timescale ($t_{th} \sim \alpha^{-1}(R_{adv}/R_S)^{3/2} M_{BH}$) for $\dot{m} = 1000$ is approximately $30(M_{BH}/[10^7 M_\odot])$ years in the rest frame (S. Zhou et al. 2024a, 2025). This duration is much longer than the timescales of current LRD monitoring campaigns (ranging from months to a few years) and is roughly consistent with the rest-frame variability timescale ($\sim$ 25 years) inferred from a gravitationally lensed LRD by Z. Zhang et al. (2025b). In addition, the hyper-Eddington accretion process is also expected to suppress the variability amplitudes (e.g., Z. Zhang et al. 2025a; A. Secunda et al. 2026). In our model, the lack of month-long variability in LRDs tentatively suggests that they are likely to host SMBHs with $M_{BH} \gg 10^5 M_\odot$.

To qualitatively predict the long-term optical variability of LRDs, we generate a mock light curve based on the hypothesis that LRDs and SS 433 share a similar variability mechanism. We use the R-band light curve of SS 433 when the accretion disk is viewed from edge-on as our baseline (upper panel of Figure 7). The R-band data are obtained from the Russian Turkish 1.5-m telescope with a median sampling interval of $\sim$ 1 s (R. A. Burenin et al. 2011). By matching the observed characteristic temperature of SS 433 (5×10^4–7×10^4 K; J. F. Dolan et al. 1997) to our estimated maximum observable temperatures derived in Section 2.2 (Figure 2), we infer a dimensionless accretion ratio of $\dot{m} \approx 626$ with fixing the black hole mass of $M_{BH} \approx 6\ M_\odot$. We then scale the time axis of the SS 433 light curve onto an LRD. The timescale scaling factor $f_{scale} = t_{th,LRD}/t_{th,SS\ 433}$ is defined as the ratio of the thermal timescales at the maximum temperature radius for both systems. The middle panel of Figure 7 shows the scaled light curve of an LRD with $M_{BH} = 10^7 M_\odot$ and $\dot{m} = 1000$. Hence, the variability timescale for the LRD is on the order of several years (rest frame).

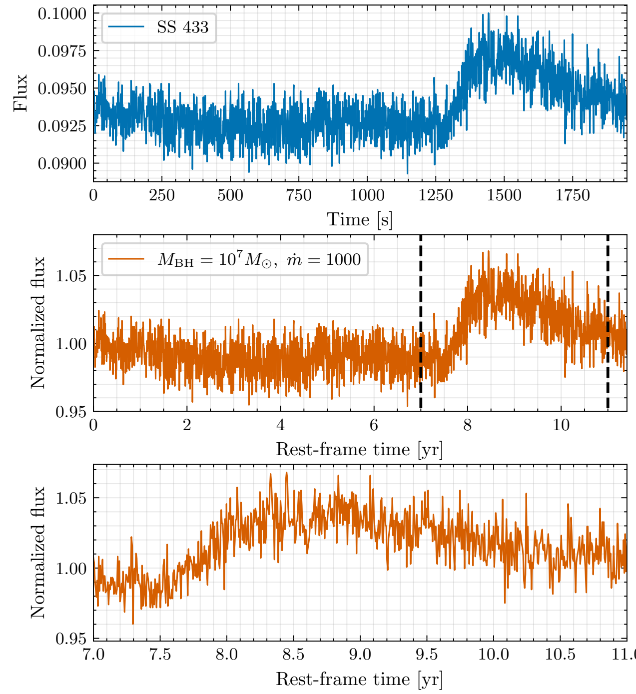

Figure 7. Mocked optical light curve of an LRD ($M_{BH} = 10^7 M_\odot$ and $\dot{m} = 1000$), derived by scaling the characteristic thermal timescale of SS 433. The upper panel displays the R-band light curve of SS 433 during a nearly edge-on view, with a median sampling interval of $\sim$ 1 s obtained by (R. A. Burenin et al. 2011). The middle panel presents the simulated LRD optical light curve, scaled by the ratio of the thermal timescales at the maximum temperature radius (Figure 2), i.e., $f_{scale} = t_{th,LRD}/t_{th,SS\ 433}$. The bottom panel provides a zoomed view of the intervals indicated by the vertical black dashed lines in the middle panel. Assuming LRDs and SS 433 share a common variability mechanism, we predict that LRDs will exhibit variability over several years in the rest frame.

UV emission from the innermost disk regions photoionizes the BLR clouds, producing the observed BELs. Within the standard reverberation-mapping framework, the BELs should respond to variability in the ionizing continuum. For an SMBH with $M_{BH} = 10^7 M_\odot$ and $\dot{m} = 1000$, the face-on luminosity of $\nu L_\nu(5100\text{Å}) \approx 10^{45}$ erg s^{-1} implies a BLR light-travel time of $\sim$ 180 days according to the R–L relation (M. C. Bentz et al. 2013). The BEL variability amplitude is naturally suppressed relative to the ionizing UV continuum due to the smoothing effect of the light-travel time across the extended BLR. For the same reason, the BEL variability timescale should be longer than that of the ionizing UV continuum. Nevertheless, the relevant timescales for BELs are still much shorter than the thermal timescale of the red optical continuum. Hence, we expect the variability of BELs to be easier to detect than that of the red optical continuum. Variations in the EWs of Hα have been observed in the local LRD 'Lord of LRDs', whereas there is no photometric variability beyond measurement uncertainties (e.g., X. Ji et al. 2026a; E. Lambrides et al. 2026). A narrow filter centered on the BELs can be used to detect BEL variability and probe the variability properties of LRDs.

In our framework, LBDs are either the same class of hyper-Eddington SMBHs seen at lower inclination or super-Eddington SMBHs with lower $\dot{m}$ (panel d in Figure 1). Therefore, since the inner disk regions are visible to the observer in these cases, LBDs should exhibit more pronounced UV/optical variability than LRDs.

If the disk scale height changes due to fluctuations in the accretion rate, one would expect a transition from an LRD to an LBD, and vice versa. The characteristic timescale for the scale height to change around the truncation radius would be the dynamical timescale, which is about $3(M_{\rm BH}/[10^7\ M_\odot])$ years in the rest frame.

2.6. *The apparent Eddington ratio*

Due to geometric self-shielding, the observed SED of an LRD is much softer than the intrinsic one. Thus, the bolometric luminosity inferred from the observed SED can be much lower than the true bolometric luminosity, leading to a substantial underestimation of the Eddington ratio $L_{\rm bol}/L_{\rm Edd}$. At high inclinations ($60° \lesssim i \lesssim 80°$), the observed isotropic (i.e., incorrectly assume the radiation is isotropic) continuum luminosity for $M_{\rm BH} = 10^7\ M_\odot$ and $\dot{m} = 1000$ at rest-frame 5100 Å is $2\times10^{43} \lesssim \nu L_\nu(5100\text{Å})/[\text{erg s}^{-1}] \lesssim 3\times10^{44}$ (Figure 4). If we adopt a bolometric correction factor of 10 for the luminosity at rest-frame 5100 Å, the apparent Eddington ratio is 0.16–3 between $60° \lesssim i \lesssim 80°$. Furthermore, if the high inclination also leads to an overestimation of $M_{\rm BH}$, then the apparent Eddington ratio would be further suppressed. In our model, hyper-Eddington LRDs can therefore appear as sub-Eddington accretion. Observational studies often use the broad Hα line luminosity to infer the bolometric luminosity (e.g., R. Maiolino et al. 2024; X. Ji et al. 2025; I. Juodžbalis et al. 2026); this conversion depends on the BLR covering factor. In our model, the BLRs of LRDs may differ from those in normal AGNs because the ionizing field of the latter is more isotropic. Therefore, the conversion of the broad Hα line to the bolometric luminosity may be different for LRDs and normal AGNs.

2.7. *The radio emission*

LRDs are often found to be radio undetected (e.g., K. Perger et al. 2025; G. Mazzolari et al. 2026). In radio-loud AGNs, the radio emission is considered to originate from relativistic jets launched from the innermost regions of the accretion disk. In the hyper-Eddington accretion case, the jet from the innermost SLIM disk can be baryonic, resulting in a lower velocity due to the high accretion rate. Indeed, the jet in SS 433 has a velocity of $\sim 0.26c$ (S. N. Fabrika et al. 2007); the jet in M81 ULS-1 has a velocity of $\sim 0.17c$ (J.-F. Liu et al. 2015). Radio emission in M81 ULS-1 is undetected, possibly due to its extragalactic distance (J.-F. Liu et al. 2015). The radio flux of SS 433 is around 1 Jy at a distance of 5 kpc (S. N. Fabrika et al. 2007). If we scale the radio flux of SS 433 by the black hole mass ratio and the square of the luminosity distance ratio, the expected radio flux for an LRD with $M_{\rm BH} = 10^7\ M_\odot$ at $z = 0.2$ ($z = 6$) is around 20 μJy (7 nJy). These estimates suggest that radio signatures from local LRD analogs should be detectable through deep Very Large Array (VLA) exposures. Indeed, radio emission is detected in the local LRD analog SDSS J104755.92+073951.2, with a radio flux of $\simeq 100\ \mu$Jy at 6.0 GHz (L. F. Rodriguez & I. F. Mirabel 2026). Meanwhile, radio emission from a high-redshift LRD may be detectable only with the Square Kilometer Array (SKA) or the FAST Core Array (P. Jiang et al. 2024).

Baryonic jets may also produce neutrinos through hadronic interactions. Therefore, neutrinos would provide a unique probe of hyper-Eddington accretion in LRDs because they can propagate through dense gas. Due to their high number density, LRDs have even been suggested as significant contributors to the diffuse neutrino background (e.g., R. Kuze et al. 2026). Future observations by neutrino telescopes could verify this idea.

3. DISCUSSION

Motivated by the observational features (softer-than-expected SED and anisotropic nature) of the hyper-Eddington X-ray binary SS 433, we propose that LRDs are hyper-Eddington accretion SMBHs ($\dot{m} \gtrsim 500$) at high inclinations. The model naturally explains the red optical continuum, the prominent Balmer break, the observed BEL properties, the X-ray weakness, the weak variability, and the apparent sub-Eddington luminosities. The key ingredient is geometric self-shielding by the puffed-up SLIM disk, which obscures the high-energy emission from the inner regions and makes the emergent SED highly inclination-dependent. This geometry naturally links LRDs and LBDs as high- and low-inclination counterparts of the same underlying accretion structure.

The origin of the UV component remains uncertain: it may be scattered inner-disk light, emission from a young stellar population, or nebular emission due to the interaction between an SS 433-like slow jet and the ambient gas. If dominated by scattered light, the UV contin-

Table 1. SMBH accretion models

Model	Gas-enshrouded AGN	BLR-attenuation	Polish donut	Spherical super-Eddington accretion	Hyper-Eddington SLIM disk
Reference	e.g., D. Kido et al. (2025); R. P. Naidu et al. (2025); M. C. Begelman & J. Dexter (2026); V. Rusakov et al. (2026); A. Sneppen et al. (2026)	K. Inayoshi & R. Maiolino (2025); X. Ji et al. (2025)	P. Madau & R. Maiolino (2026); P. Madau et al. (2026)	H. Liu et al. (2025)	This work
Central engine	Black-hole star / quasi-star / non-spherical cocoons	AGN with dense gas clumps	Super-Eddington non-advective accretion (a.k.a., Polish donut)	Super-Eddington spherical accretion	Hyper-Eddington accretion (advection dominated)
Red optical continuum	Fully-covered dense gas envelop	AGN continuum attenuated by BLR-associated dense gas + Dust reddening	Polish donut continuum attenuated by BLR-associated dense gas + Dust reddening	Spherical photosphere	Self-shielded disk photosphere (weak variability)
UV continuum	Stellar population	Attenuated AGN continuum/Stellar population	Polish donut continuum attenuated by BLR-associated dense gas + Dust reddening	—	Stellar population or nebular emission (non-variable) or scattered AGN emission (variable)?
Ionization continuum	AGN	AGN	Polish donut anisotropic emission	—	Inner anisotropic emission
Balmer break	Fully-covered dense gas envelop	BLR-associated dense gas	BLR-associated dense gas	Spherical photosphere	Self-shielded disk photosphere
Balmer absorption lines	Fully-covered dense gas envelop	BLR-associated dense gas	BLR-associated dense gas/torus	—	BLR or circumnuclear clouds?
Emission line profile	Scattering	—	Stratified BLR clouds	—	Stratified BLR clouds
X-ray weakness	Fully-covered dense gas envelop	BLR-associated dense gas obscuration	Intrinsically weak + Self-shielding	—	Intrinsically weak + Self-shielding
Radio emssion	Fully-covered dense gas envelop blocks radio emission	—	—	—	Baryonic jet

uum should be significantly polarized, with LRDs and LBDs showing similar polarized spectral signatures at a given accretion rate. The V-shaped SED can then be reproduced because the disk emission cannot extend to UV.

3.1. *Comparison to other models*

Some SMBH accretion models have been proposed to explain the nature of LRDs (see Table 1). For example, P. Madau & R. Maiolino (2026) propose that LRDs are powered by super-Eddington accretion onto SMBHs with large inclination angles, which is similar to our model. In their model, the X-ray weakness can also be explained naturally (also see, e.g., F. Pacucci & R. Narayan 2024). One major difference is that their model is based on the "Polish doughnut" model (e.g., B. Paczyński & P. J. Wiita 1980) rather than the SLIM disk. While the SLIM disk is advection-dominated, the "Polish doughnut" is constructed using a static geometric model with a presumed specific angular momentum distribution at its photosphere, rather than solving the disk equations. The scale height of the "Polish doughnut" can be much larger than R. In addition, they attribute the V-shaped SED to the joint effects of self-shielding and dust extinction, and the Balmer break to BLR gas attenuation, which differs from our model. The BLR-attenuation scenario (e.g., K. Inayoshi & R. Maiolino 2025; X. Ji et al. 2025) can be tested through the variability of the BELs and the red optical continuum. If BLR attenuation is responsible for the red optical continuum, the BELs should show the "holiday effect" (i.e., the BELs do not respond to the variability of the optical continuum), as observed in NGC 5548 (M. R. Goad et al. 2016; M. Dehghanian et al. 2019).

Another highly relevant model is the super-Eddington disk model presented by H. Liu et al. (2025), which is based on either a standard SSD or spherical accretion. The authors presented excellent radiative calculations demonstrating that the Balmer break and red continuum can be produced intrinsically by super-Eddington accretion, without invoking gas or dust attenuation. They did not consider the self-shielding effect and the anisotropic nature of the SED, which are key to explaining the observed SEDs and BELs of LRDs. They also did not mention the connection between LRDs and ULSs, which motivates this work.

Much previous work has focused on the black-hole star (e.g., D. Kido et al. 2025) or quasi-star (M. C. Begelman et al. 2008; M. C. Begelman & J. Dexter 2026) scenario. In these scenarios, an SMBH is surrounded by a large amount of gas with a temperature of ~ 5000 K (as predicted by M. C. Begelman et al. 2008), which can produce the red optical continuum and the Balmer break. The main differences between these scenarios and our model are as follows. First, the red optical continuum and the Balmer break in the black-hole star or quasi-star scenario are produced by the large amount of gas surrounding the SMBH, whereas those in our model are produced by the self-shielded thick disk. Second, the black-hole star or quasi-star scenario is based on spherical accretion, whereas our model is built upon disk hyper-Eddington accretion, which shows anisotropic emission. Third, the quasi-star scenario always predicts scatter-broadened BELs, whereas BELs in our model are emitted by BLRs.

Several works have also proposed that the V-shaped SEDs of LRDs are due to the joint contribution of an inner accretion disk and additional stellar heating in the outer self-gravitating regions. For example, C. Zhang et al. (2026) assume that the inner accretion disk is a standard SSD and that the outer self-gravity regions are heated by star formation. Meanwhile, J.-M. Wang et al. (2025a) consider the inner accretion disk to be a SLIM disk and the outer self-gravity regions to be heated by stellar-mass black hole accretion, which is motivated by disk-size studies (S. Zhou et al. 2024b; J.-M. Wang et al. 2025b). Very recently, Y.-X. Chen et al. (2026) argued that stellar objects in the outer self-gravity regions can hollow out the inner disk and that its emission is responsible for the observed universal effective temperature of ~ 5000 K; instead, the UV emission is produced by stellar populations on galaxy scales. Hence, we conclude that all three models predict extremely weak optical-continuum variability because of statistical averaging effects. The UV emission can be variable in the models of C. Zhang et al. (2026) and J.-M. Wang et al. (2025a), with the former expected to be more variable than the latter. The BELs can vary in the models of C. Zhang et al. (2026) and J.-M. Wang et al. (2025a) due to variability in the ionizing UV continuum, but not in the model of Y.-X. Chen et al. (2026) due to the lack of disk UV photons. Hence, a future time-domain joint study of the UV/optical continuum and BELs can be used to test these models and ours. We also note that additional stellar heating scenarios can be combined with our model, which may be necessary to explain the observed SEDs of some LRDs.

3.2. *SMBH mass growth*

If LRDs are indeed powered by hyper-Eddington accretion with an inflowing accretion rate of $\dot{m} \gtrsim 500$ and large inclination angles, this has important implications for SMBH mass growth in the early universe. However, due to the large inclination angles, we are unable to directly probe the inner structure of the SLIM disk and the actual accretion rate at the SMBH event horizon. The BELs from BLR clouds in the polar regions might be used to probe the ionizing continuum from the innermost regions. The inferred results would depend on the BLR geometry, which is still unclear. Reverberation-mapping observations might be of limited help because the observed optical continuum is unlikely to be a good proxy for the ionizing continuum. Spatial resolution of BLR clouds is a promising way to study them. Current GRAVITY+ observations (Gravity+ Collaboration et al. 2022) are already making progress, and next-generation interferometric facilities could provide the necessary resolution and sensitivity to resolve these distant systems.

We discuss SMBH mass growth in the early universe by considering the following two possibilities. First, the accretion rate at the event horizon of the SMBH is also $\dot{m} \gtrsim 500$. In this case, the e-folding timescale for SMBH growth by accretion would be 1/500 of the Salpeter timescale ($t_{\rm ST} \simeq 5 \times 10^7$ yrs), which is around 10^5 years. Hence, it is easy to account for the observed $M_{\rm BH}$ at redshift $z \sim 7$. Consequently, this inefficient feedback allows inflowing gas to drive hyper-Eddington accretion, thereby allowing the SMBH mass to increase ahead of the host galaxy's stellar mass. This scenario naturally explains the exceptionally high $M_{\rm BH}/M_\star$ ratios and overmassive black holes observed in LRD populations (e.g., I. Juodžbalis et al. 2025). Second, the accretion rate at the event horizon of the SMBH is only about $\dot{m} \sim 1$—10 because of strong winds in the inner regions. In this case, it would still be possible to account for the observed $M_{\rm BH}$ at redshift $z \sim 7$.

3.3. *Caveats*

It is important to acknowledge that the vertical structure of the hyper-Eddington accretion disk, as derived in Section 2.3, omits certain physical complexities, such as convection, outflows, self-illumination, and other effects that could alter the disk structures in hyper-Eddington accretion regimes. To evaluate the impact of these uncertainties on our primary results, we tested the sensitivity of the Balmer break to the vertical gas density distribution. We compare the Balmer break strength derived from our vertical density profile with that derived from a simplified case assuming a uniform gas density across the vertical dimension (see Appendix C). We find that the Balmer break remains prominent even under the simplified assumption of uniform density. This comparison shows that, although our current vertical-structure calculations may not capture all the physical details, the prediction of strong Balmer breaks is robust.

There are several simplifications in our radiative transfer calculations that should be noted. First, our calculations assume LTE. While this is a reasonable approximation for dense, optically thick regions, lower-density upper layers may exhibit non-LTE effects. These deviations could alter the ionization states and level populations of hydrogen, potentially modifying emission/absorption lines in the emergent SED. Second, our radiative transfer calculation is static and does not consider the gas kinematics within the accretion disk, which could affect the break and line profiles.

4. SUMMARY

Motivated by the softer-than-expected SED and anisotropic nature of SS 433, we propose a hyper-Eddington SMBH accretion model with $\dot{m} \gtrsim 500$ to explain the observational features of LRDs. Our results can be summarized as follows.

- The red optical continuum, with characteristic effective temperature ~ 5000 K, can arise naturally from self-shielding in the SLIM disk. We therefore interpret LRDs as high-inclination, hyper-Eddington SMBHs, with LBDs representing the low-inclination counterparts (Section 2.2; Figures 1 and 2).

- The Balmer break is produced by radiative transfer in the outer disk photosphere (Section 2.3; Figures 3 and 4). At low inclination, the break disappears, while UV photons from the inner flow can still photoionize the BLR, producing strong BELs.

- The Balmer break strength should correlate with the FWHM of the BELs through the inclination effect (Section 2.4).

- The optical continuum should show weak variability because the large accretion rate and emission-region size imply a long thermal timescale. The BELs should be more variable than the red optical continuum, and the variability of the two components may not be tightly correlated (Section 2.5).

- Because the observed SED is much softer than the intrinsic one, $L_{\rm bol}/L_{\rm Edd}$ can substantially underestimate the true Eddington ratio (Section 2.6).

According to our model, the LRD phase terminates once the SMBH undergoes significant mass growth and the gas supply can no longer sustain the required high $\dot{m}$. If confirmed, this picture would have important implications for SMBH growth in the early universe (Section 3.2). In particular, it can accommodate the observed $M_{\rm BH}$ at $z \sim 7$ even if the accretion rate at the event horizon is only $\dot{m} \sim 10$. Future JWST multi-epoch observations of LRDs can directly test our model predictions, thereby revealing the key mass growth phase in SMBHs.

ACKNOWLEDGEMENTS

We thank J.-M. Wang and X. Cao for their helpful discussions. M.Y.S. and S.Y.Z. acknowledge support from the National Natural Science Foundation of China (NSFC-12322303, NSFC-125B2058, NSFC-12533006), the National Key R&D Program of China (No. 2023YFA1607903), and the Fundamental Research Funds for the Central Universities (20720240152). Y.P.L. was supported by the National Natural Science Foundation of China (grants 12373070, and 12192223). LCH was supported by the National Science Foundation of China (12233001) and the China Manned Space Program (CMS-CSST-2025-A09). W.M.G. acknowledges support from the National Natural Science Foundation of China (NSFC-12221003), the National Key R&D Program of China (No. 2023YFA1607901) and the China Manned Space Program (CMS-CSST-2025-A13). This manuscript benefited from grammar checking by `Gemma`. We acknowledge the DAWN JWST Archive (DJA) for providing the reduced data products.

AUTHOR CONTRIBUTIONS

REFERENCES

Abramowicz, M. A., Czerny, B., Lasota, J. P., & Szuszkiewicz, E. 1988, ApJ, 332, 646, doi: 10.1086/166683

Akins, H. B., Casey, C. M., Lambrides, E., et al. 2025, ApJ, 991, 37, doi: 10.3847/1538-4357/ade984

Ando, M., Harikane, Y., Katz, H., Inayoshi, K., & Tanaka, T. S. 2026, arXiv e-prints, arXiv:2606.03522, doi: 10.48550/arXiv.2606.03522

Begelman, M. C. 1978, MNRAS, 184, 53, doi: 10.1093/mnras/184.1.53

Begelman, M. C., & Dexter, J. 2026, ApJ, 996, 48, doi: 10.3847/1538-4357/ae274a

Begelman, M. C., King, A. R., & Pringle, J. E. 2006, MNRAS, 370, 399, doi: 10.1111/j.1365-2966.2006.10469.x

Begelman, M. C., Rossi, E. M., & Armitage, P. J. 2008, MNRAS, 387, 1649, doi: 10.1111/j.1365-2966.2008.13344.x

Begelman, M. C., & Volonteri, M. 2017, MNRAS, 464, 1102, doi: 10.1093/mnras/stw2446

Bentz, M. C., Denney, K. D., Grier, C. J., et al. 2013, ApJ, 767, 149, doi: 10.1088/0004-637X/767/2/149

Berton, M., Björklund, I., Lähteenmäki, A., et al. 2020, Contributions of the Astronomical Observatory Skalnate Pleso, 50, 270, doi: 10.31577/caosp.2020.50.1.270

Bogdán, Á., Goulding, A. D., Natarajan, P., et al. 2024, Nature Astronomy, 8, 126, doi: 10.1038/s41550-023-02111-9

Brammer, G., & Valentino, F. 2025, The DAWN JWST Archive: Compilation of Public NIRSpec Spectra, 4.4 Zenodo, doi: 10.5281/zenodo.15472354

Brazzini, M., D'Eugenio, F., Maiolino, R., et al. 2025, MNRAS, 544, L167, doi: 10.1093/mnrasl/slaf116

Brazzini, M., D'Eugenio, F., Maiolino, R., et al. 2026, arXiv e-prints, arXiv:2601.22214, doi: 10.48550/arXiv.2601.22214

Bunker, A. J., Cameron, A. J., Curtis-Lake, E., et al. 2024, A&A, 690, A288, doi: 10.1051/0004-6361/202347094

Burenin, R. A., Revnivtsev, M. G., Khamitov, I. M., et al. 2011, Astronomy Letters, 37, 100, doi: 10.1134/S1063773711010026

Calzetti, D., Armus, L., Bohlin, R. C., et al. 2000, ApJ, 533, 682, doi: 10.1086/308692

Castor, J. I., Abbott, D. C., & Klein, R. I. 1975, ApJ, 195, 157, doi: 10.1086/153315

Chang, S.-J., Gronke, M., Matthee, J., & Mason, C. 2026, MNRAS, 545, staf2131, doi: 10.1093/mnras/staf2131

Chen, C.-H., Ho, L. C., Li, R., & Inayoshi, K. 2025, ApJL, 989, L12, doi: 10.3847/2041-8213/adee0a

Chen, C.-H., Shangguan, J., Ho, L. C., et al. 2026, arXiv e-prints, arXiv:2606.04711, doi: 10.48550/arXiv.2606.04711

Chen, K., Li, Z., Inayoshi, K., & Ho, L. C. 2025, ApJL, 994, L42, doi: 10.3847/2041-8213/ae1955

Chen, Y.-X., Liu, H., Li, R., et al. 2026, arXiv e-prints, arXiv:2602.06954, doi: 10.48550/arXiv.2602.06954

Cherepashchuk, A. M. 1981, MNRAS, 194, 761, doi: 10.1093/mnras/194.3.761

Cherepashchuk, A. M., Postnov, K. A., & Belinski, A. A. 2019, MNRAS, 485, 2638, doi: 10.1093/mnras/stz610

de Graaff, A., Hviding, R. E., Naidu, R. P., et al. 2025a, arXiv e-prints, arXiv:2511.21820, doi: 10.48550/arXiv.2511.21820

de Graaff, A., Rix, H.-W., Naidu, R. P., et al. 2025b, A&A, 701, A168, doi: 10.1051/0004-6361/202554681

de Graaff, A., Brammer, G., Weibel, A., et al. 2025c, A&A, 697, A189, doi: 10.1051/0004-6361/202452186

Dehghanian, M., Ferland, G. J., Peterson, B. M., et al. 2019, ApJL, 882, L30, doi: 10.3847/2041-8213/ab3d41

D'Eugenio, F., Cameron, A. J., Scholtz, J., et al. 2025, ApJS, 277, 4, doi: 10.3847/1538-4365/ada148

Dolan, J. F., Boyd, P. T., Fabrika, S., et al. 1997, A&A, 327, 648

Done, C., Gierliński, M., & Kubota, A. 2007, A&A Rv, 15, 1, doi: 10.1007/s00159-007-0006-1

Du, P., Lu, K.-X., Hu, C., et al. 2016, ApJ, 820, 27, doi: 10.3847/0004-637X/820/1/27

Eikenberry, S. S., Cameron, P. B., Fierce, B. W., et al. 2001, ApJ, 561, 1027, doi: 10.1086/323380

Eisenstein, D. J., Willott, C., Alberts, S., et al. 2026, ApJS, 283, 6, doi: 10.3847/1538-4365/ae3163

Fabrika, S. N., Abolmasov, P. K., & Karpov, S. 2007, in IAU Symposium, Vol. 238, Black Holes from Stars to Galaxies – Across the Range of Masses, ed. V. Karas & G. Matt, 225–228, doi: 10.1017/S1743921307005017

Fabrika, S. N., & Sholukhova, O. 2008, in Microquasars and Beyond, 52, doi: 10.22323/1.062.0052

Furtak, L. J., Labbé, I., Zitrin, A., et al. 2024, Nature, 628, 57, doi: 10.1038/s41586-024-07184-8

Gayley, K. G. 1995, ApJ, 454, 410, doi: 10.1086/176492

Gies, D. R., McSwain, M. V., Riddle, R. L., et al. 2002, ApJ, 566, 1069, doi: 10.1086/338335

Goad, M. R., Korista, K. T., De Rosa, G., et al. 2016, ApJ, 824, 11, doi: 10.3847/0004-637X/824/1/11

Gravity+ Collaboration, Abuter, R., Alarcon, P., et al. 2022, The Messenger, 189, 17, doi: 10.18727/0722-6691/5285

Greene, J. E., Labbe, I., Goulding, A. D., et al. 2024, ApJ, 964, 39, doi: 10.3847/1538-4357/ad1e5f

Gu, W.-M. 2012, ApJ, 753, 118, doi: 10.1088/0004-637X/753/2/118

Gu, W.-M., Sun, M.-Y., Lu, Y.-J., Yuan, F., & Liu, J.-F. 2016, ApJL, 818, L4, doi: 10.3847/2041-8205/818/1/L4

Gu, W.-M., Xue, L., Liu, T., & Lu, J.-F. 2009, PASJ, 61, 1313, doi: 10.1093/pasj/61.6.1313

Harikane, Y., Zhang, Y., Nakajima, K., et al. 2023, ApJ, 959, 39, doi: 10.3847/1538-4357/ad029e

Heintz, K. E., Brammer, G. B., Watson, D., et al. 2025, A&A, 693, A60, doi: 10.1051/0004-6361/202450243

Hirose, S., Krolik, J. H., & Blaes, O. 2009, ApJ, 691, 16, doi: 10.1088/0004-637X/691/1/16

Inayoshi, K., Haiman, Z., & Ostriker, J. P. 2016, MNRAS, 459, 3738, doi: 10.1093/mnras/stw836

Inayoshi, K., & Maiolino, R. 2025, ApJL, 980, L27, doi: 10.3847/2041-8213/adaebd

Ivey, L. R., D'Eugenio, F., Maiolino, R., et al. 2026, arXiv e-prints, arXiv:2604.09177, doi: 10.48550/arXiv.2604.09177

Ji, X., Maiolino, R., Übler, H., et al. 2025, MNRAS, 544, 3900, doi: 10.1093/mnras/staf1867

Ji, X., D'Eugenio, F., Juodžbalis, I., et al. 2026a, MNRAS, 545, staf2235, doi: 10.1093/mnras/staf2235

Ji, X., Pezzulli, G., D'Eugenio, F., et al. 2026b, arXiv e-prints, arXiv:2604.03370, doi: 10.48550/arXiv.2604.03370

Jiang, P., Chen, R., Gan, H., et al. 2024, Astronomical Techniques and Instruments, 1, 84, doi: 10.61977/ati2024012

Juodžbalis, I., Ji, X., Maiolino, R., et al. 2024, MNRAS, 535, 853, doi: 10.1093/mnras/stae2367

Juodžbalis, I., Marconcini, C., D'Eugenio, F., et al. 2025, arXiv e-prints, arXiv:2508.21748, doi: 10.48550/arXiv.2508.21748

Juodžbalis, I., Maiolino, R., Baker, W. M., et al. 2026, MNRAS, 546, stag086, doi: 10.1093/mnras/stag086

Kaaret, P., Feng, H., & Roberts, T. P. 2017, ARA&A, 55, 303, doi: 10.1146/annurev-astro-091916-055259

Kato, S., Fukue, J., & Mineshige, S. 2008, Black-Hole Accretion Disks — Towards a New Paradigm —

Kido, D., Ioka, K., Hotokezaka, K., Inayoshi, K., & Irwin, C. M. 2025, MNRAS, 544, 3407, doi: 10.1093/mnras/staf1898

King, A., Lasota, J.-P., & Middleton, M. 2023, NewAR, 96, 101672, doi: 10.1016/j.newar.2022.101672

King, A. R., & Pounds, K. A. 2003, MNRAS, 345, 657, doi: 10.1046/j.1365-8711.2003.06980.x

King, A. R., Taam, R. E., & Begelman, M. C. 2000, ApJL, 530, L25, doi: 10.1086/312475

Kocevski, D. D., Onoue, M., Inayoshi, K., et al. 2023, ApJL, 954, L4, doi: 10.3847/2041-8213/ace5a0

Kuze, R., Ioka, K., Murase, K., Kimura, S. S., & Inayoshi, K. 2026, arXiv e-prints, arXiv:2601.11203, doi: 10.48550/arXiv.2601.11203

Labbe, I., Greene, J. E., Matthee, J., et al. 2024, arXiv e-prints, arXiv:2412.04557, doi: 10.48550/arXiv.2412.04557

Lambrides, E., Hutchison, T. A., Larson, R. L., et al. 2026, arXiv e-prints, arXiv:2604.25991, doi: 10.48550/arXiv.2604.25991

Li, J., Silverman, J. D., Shen, Y., et al. 2025, ApJ, 981, 19, doi: 10.3847/1538-4357/ada603

Lin, X., Fan, X., Cai, Z., et al. 2026a, ApJ, 997, 364, doi: 10.3847/1538-4357/ae2bdf

Lin, X., Fan, X., Cai, Z., et al. 2026b, arXiv e-prints, arXiv:2605.21574, doi: 10.48550/arXiv.2605.21574

Liu, H., Jiang, Y.-F., Quataert, E., Greene, J. E., & Ma, Y. 2025, ApJ, 994, 113, doi: 10.3847/1538-4357/ae0c19

Liu, J.-F., Bai, Y., Wang, S., et al. 2015, Nature, 528, 108, doi: 10.1038/nature15751

Madau, P., & Haardt, F. 2024, ApJL, 976, L24, doi: 10.3847/2041-8213/ad90e1

Madau, P., & Maiolino, R. 2026, arXiv e-prints, arXiv:2602.22386, doi: 10.48550/arXiv.2602.22386

Madau, P., Maiolino, R., Scholtz, J., & D'Eugenio, F. 2026, arXiv e-prints, arXiv:2604.04216, doi: 10.48550/arXiv.2604.04216

Maiolino, R., Scholtz, J., Curtis-Lake, E., et al. 2024, A&A, 691, A145, doi: 10.1051/0004-6361/202347640

Maiolino, R., Risaliti, G., Signorini, M., et al. 2025, MNRAS, 538, 1921, doi: 10.1093/mnras/staf359

Maiolino, R., Übler, H., D'Eugenio, F., et al. 2026, MNRAS, 548, staf2109, doi: 10.1093/mnras/staf2109

Margon, B., & Anderson, S. F. 1989, ApJ, 347, 448, doi: 10.1086/168132

Matthee, J., Torralba, A., Pezzulli, G., et al. 2026, arXiv e-prints, arXiv:2603.17667, doi: 10.48550/arXiv.2603.17667

Mazzolari, G., Gilli, R., Maiolino, R., et al. 2026, A&A, 706, A372, doi: 10.1051/0004-6361/202453317

Middleton, M. J., Walton, D. J., Alston, W., et al. 2021, MNRAS, 506, 1045, doi: 10.1093/mnras/stab1280

Mihalas, D., Auer, L. H., & Mihalas, B. R. 1978, ApJ, 220, 1001, doi: 10.1086/155988

Morag, J. 2025a, jon-morag/Freq_Dept_Opac_Table: NuPac - 2.1, v2.1 Zenodo, doi: 10.5281/zenodo.17935053

Morag, J. 2025b, arXiv e-prints, arXiv:2509.17003, doi: 10.48550/arXiv.2509.17003

Naidu, R. P., Matthee, J., Katz, H., et al. 2025, arXiv e-prints, arXiv:2503.16596, doi: 10.48550/arXiv.2503.16596

Pacucci, F., Ferrara, A., & Kocevski, D. D. 2026, arXiv e-prints, arXiv:2601.14368, doi: 10.48550/arXiv.2601.14368

Pacucci, F., & Narayan, R. 2024, ApJ, 976, 96, doi: 10.3847/1538-4357/ad84f7

Paczyńsky, B., & Wiita, P. J. 1980, A&A, 88, 23

Perger, K., Fogasy, J., Frey, S., & Gabányi, K. É. 2025, A&A, 693, L2, doi: 10.1051/0004-6361/202452422

Perna, M., Arribas, S., Marshall, M., et al. 2023, A&A, 679, A89, doi: 10.1051/0004-6361/202346649

Pollock, C. L., Gottumukkala, R., Heintz, K. E., et al. 2026, A&A, 708, A203, doi: 10.1051/0004-6361/202556032

Proga, D. 1999, MNRAS, 304, 938, doi: 10.1046/j.1365-8711.1999.02408.x

Rieke, M. J., Robertson, B., Tacchella, S., et al. 2023, ApJS, 269, 16, doi: 10.3847/1538-4365/acf44d

Rodriguez, L. F., & Mirabel, I. F. 2026, A&A, 707, L17, doi: 10.1051/0004-6361/202558326

Rusakov, V., Watson, D., Nikopoulos, G. P., et al. 2026, Nature, 649, 574, doi: 10.1038/s41586-025-09900-4

Scholtz, J., Carniani, S., Parlanti, E., et al. 2025, arXiv e-prints, arXiv:2510.01034, doi: 10.48550/arXiv.2510.01034

Scholtz, J., D'Eugenio, F., Maiolino, R., et al. 2026, arXiv e-prints, arXiv:2603.22277. https://arxiv.org/abs/2603.22277

Secunda, A., Somerville, R. S., Jiang, Y.-F., et al. 2026, ApJ, 996, 6, doi: 10.3847/1538-4357/ae1f08

Shakura, N. I., & Sunyaev, R. A. 1973, A&A, 24, 337

Shen, R.-F., Barniol Duran, R., Nakar, E., & Piran, T. 2015, MNRAS, 447, L60, doi: 10.1093/mnrasl/slu183

Sneppen, A., Watson, D., Matthews, J. H., et al. 2026, arXiv e-prints, arXiv:2601.18864, doi: 10.48550/arXiv.2601.18864

Soria, R., & Kong, A. 2016, MNRAS, 456, 1837, doi: 10.1093/mnras/stv2671

Sun, W. Q., Naidu, R. P., Matthee, J., et al. 2026, arXiv e-prints, arXiv:2601.20929, doi: 10.48550/arXiv.2601.20929

Tang, M., Stark, D. P., Plat, A., et al. 2025, ApJ, 991, 217, doi: 10.3847/1538-4357/adfd57

Torralba, A., Matthee, J., Weibel, A., et al. 2026, arXiv e-prints, arXiv:2603.28335, doi: 10.48550/arXiv.2603.28335

Trefoloni, B., Ji, X., Maiolino, R., et al. 2025, A&A, 700, A203, doi: 10.1051/0004-6361/202452795

Valentino, F., Heintz, K. E., Brammer, G., et al. 2025, A&A, 699, A358, doi: 10.1051/0004-6361/202553908

van den Heuvel, E. P. J. 1981, Vistas in Astronomy, 25, 95, doi: 10.1016/0083-6656(81)90050-7

Wang, B., Leja, J., de Graaff, A., et al. 2024, ApJL, 969, L13, doi: 10.3847/2041-8213/ad55f7

Wang, J.-M., Qiu, J., Du, P., & Ho, L. C. 2014, ApJ, 797, 65, doi: 10.1088/0004-637X/797/1/65

Wang, J.-M., & Zhou, Y.-Y. 1999, ApJ, 516, 420, doi: 10.1086/307080

Wang, J.-M., Wang, Y.-L., Chen, Y.-J., et al. 2025a, arXiv e-prints, arXiv:2511.09278, doi: 10.48550/arXiv.2511.09278

Wang, J.-M., Hu, C., Chen, Y.-J., et al. 2025b, arXiv e-prints, arXiv:2511.07716, doi: 10.48550/arXiv.2511.07716

Watarai, K.-Y., Ohsuga, K., Takahashi, R., & Fukue, J. 2005, PASJ, 57, 513, doi: 10.1093/pasj/57.3.513

Williams, R. E. 1980, ApJ, 235, 939, doi: 10.1086/157698

Zhang, C., Wu, Q., Fan, X., et al. 2026, Nature Astronomy, doi: 10.1038/s41550-026-02785-x

Zhang, L., Stone, J. M., White, C. J., et al. 2025, arXiv e-prints, arXiv:2509.10638, doi: 10.48550/arXiv.2509.10638

Zhang, Z., Jiang, L., Liu, W., & Ho, L. C. 2025a, ApJ, 985, 119, doi: 10.3847/1538-4357/adcb3e

Zhang, Z., Li, M., Oguri, M., et al. 2025b, arXiv e-prints, arXiv:2512.05180, doi: 10.48550/arXiv.2512.05180

Zhou, H., Wang, T., Yuan, W., et al. 2006, ApJS, 166, 128, doi: 10.1086/504869

Zhou, S., Sun, M., Cai, Z.-Y., et al. 2024a, ApJ, 966, 8, doi: 10.3847/1538-4357/ad2fbc

Zhou, S., Sun, M., Liu, T., et al. 2024b, ApJL, 966, L9, doi: 10.3847/2041-8213/ad3c3f

Zhou, S., Sun, M., Zhang, Z., Chen, J., & Ho, L. C. 2025, ApJ, 991, 137, doi: 10.3847/1538-4357/adfd5f

Zhuang, M.-Y., Li, J., Shen, Y., et al. 2026, ApJ, 999, 31, doi: 10.3847/1538-4357/ae3612

APPENDIX

A. DISK VERTICAL STRUCTURE

We solve the vertical structure of the accretion disk by solving the hydrostatic equilibrium, energy balance, and radiative transfer equations. These equations are given by

$$\frac{dP_{\rm tot}}{dz} = -\rho\Omega_{\rm K}^2 z, \tag{A1}$$

$$\frac{dF}{dz} = q_{\rm rad} = q_{\rm vis} - q_{\rm adv}, \tag{A2}$$

$$\frac{dT}{dz} = -\frac{3\kappa_{\rm R}\rho F}{16\sigma_{\rm SB}T^3}, \tag{A3}$$

where $P_{\rm tot}$ is the total pressure, $\Omega_{\rm K}$ is the Keplerian angular velocity, F is the radiative flux, $q_{\rm rad}$ is the radiative cooling rate, $q_{\rm vis}$ is the viscous heating rate, $q_{\rm adv}$ is the advective cooling rate, and z is the vertical distance measured from the disk midplane. These equations can be regarded as the generalized version of the thin disk model in H. Liu et al. (2025). Here, we assume that radiation pressure dominates over gas pressure ($P_{\rm tot} = P_{\rm rad}$), which is valid in the outer regions of the SLIM disk. For radiative transport, we neglect convection; this assumption should be tested by future simulations. The boundary conditions are set as $F(z=0)=0$, $F(z=H)=\sigma_{\rm SB}T_{\rm eff}^4$, and $P_{\rm rad}(z=H) = 2\sigma_{\rm SB}T_{\rm eff}^4/(3c)$, where H is the disk scale height. Following N. I. Shakura & R. A. Sunyaev (1973), we adopt the α-viscosity prescription,

$$2\alpha\int_0^H P_{\rm tot}dz = \frac{1}{2\pi}\Omega_{\rm K}\dot{M}f, \tag{A4}$$

where α is the dimensionless viscosity parameter. In our simulations, we adopt a fiducial value of $\alpha = 0.1$ unless otherwise specified. These equations can also be applied to an SSD by fixing $q_{\rm adv} = 0$. Note that Eq. A2 ensures the vertically integrated radiative cooling rate, $\int_0^H q_{\rm rad}dz = F(z=H) - F(z=0) = \sigma_{\rm SB}T_{\rm eff}^4$, is smaller than (for the SLIM solution; see Eq. 3) or identical to (for the SSD solution; see Eq. 1) the vertically integrated viscous heating rate $\int_0^H q_{\rm vis}dz = (3GM_{\rm BH}\dot{M}f)/(8\pi R^3)$. Eqs. A1–A4 are numerically challenging to solve due to the strong coupling among the equations and the extreme sensitivity of the opacity to temperature. We aim to obtain an approximate solution by following the methodology presented in the first appendix of H. Liu et al. (2025). The key procedure is to first solve the equations by assuming a constant opacity (e.g., $\kappa_{\rm R} = \kappa_{\rm es} = 0.34$ cm^2 g^{-1}) to obtain the vertical structures of $\rho(z)$, $T(z)$, and $F(z)$. Then, we fix the profiles of $\rho(z)$, $T(z)$, and $F(z)$ and allow the normalization factor of the $\rho(z)$ profile to be a free parameter. Here, we again assume that $q_{\rm rad}/q_{\rm vis}$ is independent of z and that $q_{\rm vis} \propto \kappa_{\rm R}\rho\tau^{-0.5}$ (S. Hirose et al. 2009; H. Liu et al. 2025). We can then solve Eq. A4 again with the realistic opacity table to obtain the normalization factors.

B. RADIATIVE TRANSFER IN THE DISK

We have developed a numerical framework to compute the emergent spectral energy distributions (SEDs) of accretion disks by solving the frequency-dependent radiative transfer equation in a two-dimensional (r, z) configuration. The vertical structures of gas density $\rho(r, z)$ and temperature $T(r, z)$ are pre-calculated with the hydrostatic equilibrium, radiative energy transport, thermal equilibrium, and α–viscosity prescription as detailed in Appendix A and Figure 3. As the original data are non-uniformly sampled, we use interpolation in logarithmic space to map these quantities onto a uniform global grid. The radial grid spans from $r_{\rm min} = 10R_{\rm S}$ to the self-gravity stability radius $r_{\rm max} = R_{\rm stable}$, which is defined as Toomre $Q(R_{\rm stable}) = \Omega_{\rm K}^2/2\pi G\rho \approx 1$. The vertical grid covers the range $0 \leq z \leq Z_{\rm max}$, where $Z_{\rm max}$ is defined as the maximum vertical extent of the disk structure across the entire radial range. For regions outside the disk surface, i.e., $Z_{\rm surface} \leq z \leq Z_{\rm max}$, we add a artificially small density of 10^{-30} g cm^{-3} and a temperature of 15 K. The frequency-dependent absorption opacities ($\kappa_{{\rm abs},\nu}$) and electron scattering opacities ($\kappa_{\rm es}$) are obtained from a high-resolution opacity table with a low-metallicity $Z = 0.005Z_\odot$ (J. Morag 2025a,b). For the low-density regions, the true absorption and electron scattering opacities are fixed to be 10^{-27} cm^2 g^{-1} and 10^{-29} cm^2 g^{-1}, respectively, making their contribution to the total optical depths negligible.

The radiation field is determined by solving the frequency-dependent radiative transfer equation,

$$\frac{dI_\nu}{ds} = \chi_\nu (S_\nu - I_\nu), \tag{B5}$$

where I_ν is the specific intensity, S_ν is the source function, ds is the path length along a ray, and $\chi_\nu = \rho(\kappa_{\mathrm{abs},\nu} + \kappa_{\mathrm{es}})$ is the total extinction coefficient. We use a short-characteristics (SC) ray-tracing scheme (e.g., D. Mihalas et al. 1978) on the (r, z) plane. For a given ray direction $\mathbf{n}$, the intensity I_ν at a grid point is calculated by integrating the source function from an upstream intersection point on the cell boundary. To address the potential exponential gradients in the disk atmosphere, we use logarithmic interpolation for χ_ν, S_ν, and I_ν at cell interfaces. The optical depth increment $\Delta\tau$ along a segment Δs is computing using a logarithmic average,

$$\Delta\tau = \Delta s \frac{\chi_{\mathrm{loc}} - \chi_{\mathrm{up}}}{\ln(\chi_{\mathrm{loc}}/\chi_{\mathrm{up}})}, \tag{B6}$$

where assuming $\chi = \chi_{\mathrm{up}} e^{s \cdot \ln(\chi_{\mathrm{loc}}/\chi_{\mathrm{up}})/\Delta s}$ along Δs, with χ_{up} and χ_{loc} denoting the total extinction coefficients at the upstream and local points, respectively. The emergent intensity from a cell is then obtained via the formal solution,

$$I_{\mathrm{loc}} = I_{\mathrm{up}} e^{-\Delta\tau} + \int_0^{\Delta\tau} S(\tau') e^{-(\Delta\tau - \tau')} d\tau' = I_{\mathrm{up}} e^{-\Delta\tau} + S_{\mathrm{up}} w_0 + S_{\mathrm{loc}} w_1, \tag{B7}$$

where weights $w_0 = \frac{1-e^{-\Delta\tau}}{\Delta\tau} - e^{-\Delta\tau}$ and $w_1 = 1 - \frac{1-e^{-\Delta\tau}}{\Delta\tau}$.

To account for isotropic electron scattering, the source function S_ν is coupled to the mean intensity $J_\nu = \frac{1}{4\pi} \oint I_\nu d\Omega$,

$$S_\nu = (1 - \epsilon_\nu) J_\nu + \epsilon_\nu B_\nu(T), \tag{B8}$$

where $B_\nu(T)$ is the Planck function and $\epsilon_\nu = \kappa_{\mathrm{abs},\nu}/(\kappa_{\mathrm{abs},\nu} + \kappa_{\mathrm{es}})$. We solve this coupled system using the Lambda-iteration method. In each iteration, we perform a global sweep of rays across the (r, z) grid for a discrete set of angles θ defined by Gauss-Legendre quadrature. We set boundary conditions at the midplane ($z = 0$) and the inner radial boundary ($r = r_{\mathrm{min}}$) as $I_\nu = B_\nu$. Convergence is achieved when the maximum relative change in the source function falls below 10^{-3}.

Once the source function has converged, we can compute the observable flux for various inclination angles i_{obs}. For each line of sight, we perform a final ray-trace to extract the emergent intensity $I_\nu(r, i_{\mathrm{obs}})$ at the Z_{max}. The observed flux is composed of the near and far sides of the disk (relative to the observer; see Figure 8). For the near side of the disk, the innermost radius (r_{near}) is defined as the radius at which radiation can radially escape the advective flow (see Section 2.2); this parameter has very limited impact on our final results. For the far side, the visible radius (r_{far}) is the innermost radius, below which the disk emission is shielded by the near-side SLIM disk. The total monochromatic luminosity L_ν is then obtained by integrating the intensity over the visible surface area,

$$L_\nu = \int_{r_{\mathrm{near}}}^{r_{\mathrm{max}}} \pi I_{\nu,\mathrm{near}}(r, i_{\mathrm{obs}}) r \cos i_{\mathrm{obs}} dr + \int_{r_{\mathrm{far}}}^{r_{\mathrm{max}}} \pi I_{\nu,\mathrm{far}}(r, i_{\mathrm{obs}}) r \cos i_{\mathrm{obs}} dr. \tag{B9}$$

We expect that $I_{\nu,\mathrm{far}}(r, i_{\mathrm{obs}}) = I_{\nu,\mathrm{near}}(r, -i_{\mathrm{obs}})$. The isotropic luminosity is defined as $4\pi\nu L_\nu$ to compare with observations.

C. BALMER BREAK TESTS

We investigate the sensitivity of the Balmer break strength to the viscosity parameter by comparing our fiducial model ($\alpha = 0.1$) with a lower viscosity case ($\alpha = 0.01$). As shown in Figure 9, a smaller viscosity parameter results in a more pronounced Balmer break by changing the disk vertical structure.

We also compare the nonuniform vertical density profile with a simplified uniform case to test the robustness of the Balmer break. To do so, we enforce a constant density ($\rho = \mathrm{const}$) in Eq. A1, re-calculate the vertical structure, and subsequently derive the emergent SED. As shown in Figure 10, the Balmer break remains prominent under the extreme assumption of a uniform vertical density distribution.

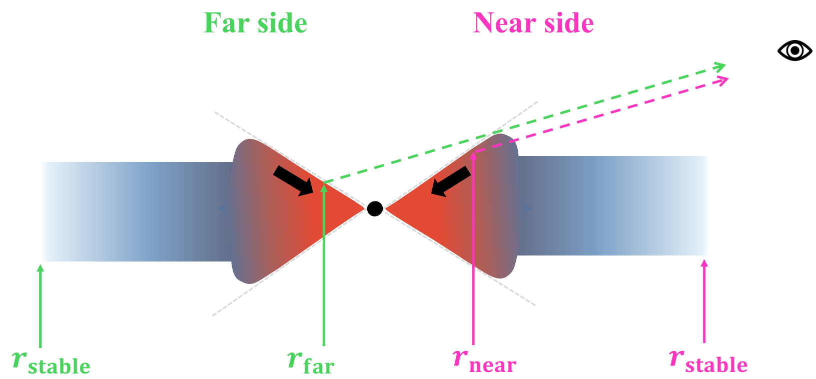

Figure 8. Schematic illustration of the disk visible surface. The observable region is bounded by: (i) the near-side innermost radius r_{near}, where photons escape the advective flow; (ii) the far-side innermost visible radius r_{far}, determined by the geometric self-shadowing of the inflated SLIM disk; and (iii) the outer boundary r_{stable}, dictated by the self-gravitational stability limit.

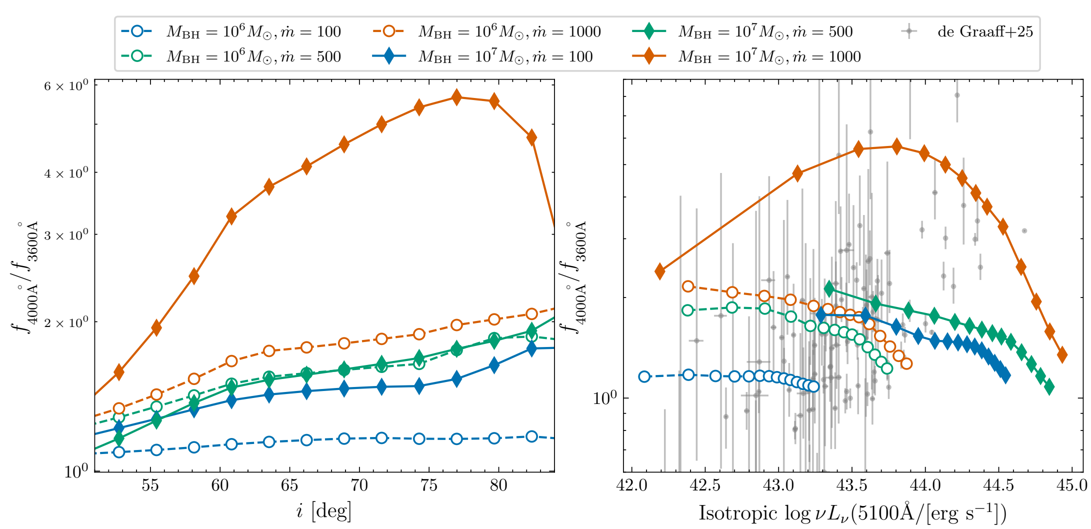

Figure 9. Same as Figure 6, but with a viscosity parameter of $\alpha = 0.01$. The modification to the vertical structure of the disk, driven by the change in viscosity, results in a more pronounced Balmer break strength.

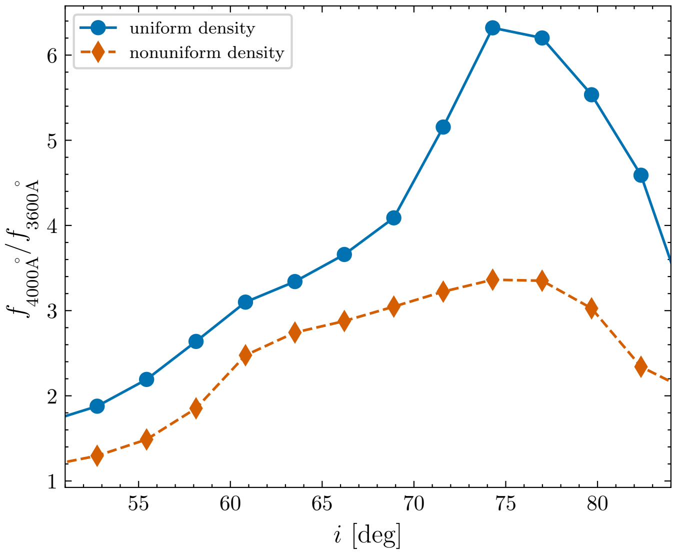

Figure 10. Comparison of Balmer break strength between models assuming a simplified uniform vertical gas density versus a realistic nonuniform vertical density profile. Orange diamonds denote the results for nonuniform vertical density (the same markers in Figure 6), while the blue dots represent the simplified, uniform density case. Even under the simplified assumption of uniform density, the Balmer break remains prominent. Consequently, while the vertical structures derived in Section 2.3 omit certain physical complexities, the fundamental prediction of the Balmer break is robust.